https://doi.org/10.1038/s44303-024-00014-6

Personalized coronary and myocardial blood flow models incorporating CT perfusion imaging and synthetic vascular trees

Karthik Menon[1,2], Muhammed Owais Khan[3], Zachary A. Sexton[4], Jakob Richter[1], Patricia K. Nguyen[5,6], Sachin B. Malik[5], Jack Boyd[7], Koen Nieman[6,8] & Alison L. Marsden[1,2,4] ✉

Computational simulations of coronary artery blood flow, using anatomical models based on clinical imaging, are an emerging non-invasive tool for personalized treatment planning. However, current simulations contend with two related challenges – incomplete anatomies in image-based models due to the exclusion of arteries smaller than the imaging resolution, and the lack of personalized flow distributions informed by patient-specific imaging. We introduce a data-enabled, personalized and multi-scale flow simulation framework spanning large coronary arteries to myocardial microvasculature. It includes image-based coronary anatomies combined with synthetic vasculature for arteries below the imaging resolution, myocardial blood flow simulated using Darcy models, and systemic circulation represented as lumped-parameter networks. We propose an optimization-based method to personalize multiscale coronary flow simulations by assimilating clinical CT myocardial perfusion imaging and cardiac function measurements to yield patient-specific flow distributions and model parameters. Using this proof-of-concept study on a cohort of six patients, we reveal substantial differences in flow distributions and clinical diagnosis metrics between the proposed personalized framework and empirical methods based purely on anatomy; these errors cannot be predicted a priori. This suggests virtual treatment planning tools would benefit from increased personalization informed by emerging imaging methods.

Coronary artery disease (CAD) is the leading cause of death worldwide[1,2]. It causes narrowing or occlusion of coronary arteries, which can lead to myocardial infarction and loss of contractile heart function. Although clinical interventions such as stenting or coronary artery bypass graft (CABG) surgery can restore coronary flow, long-term outcomes remain unsatisfactory. While CABG improves mortality and morbidity in patients with severe CAD[3–5], 24% of patients report chest pain within a year[6] and 50% of vein grafts exhibit significant stenosis within 10 years[7]. However, randomized clinical trials have shown that clinical interventions guided by hemodynamic functional metrics, such as fractional flow reserve (FFR)[8] and myocardial perfusion imaging[9–12], lead to improved outcomes, less unnecessary revascularization, and lower costs[13–18]. This is likely because CAD severity assessed using anatomical imaging correlates poorly with the functional severity and myocardial ischemic risk[19,20].

Computational fluid dynamics (CFD) simulations of coronary blood flow using anatomical image-based models are an emerging non-invasive method for hemodynamics-based risk assessment and treatment planning[21]. Clinical trials involving the FDA-approved FFR_{CT}, which uses patient-specific CFD to non-invasively compute FFR[22], have demonstrated increased diagnostic accuracy compared to anatomical imaging and a

[1]Department of Pediatrics (Cardiology), Stanford School of Medicine, Stanford, CA, USA. [2]Institute for Computational and Mathematical Engineering, Stanford University, Stanford, CA, USA. [3]Department of Electrical, Computer, and Biomedical Engineering, Toronto Metropolitan University, Toronto, ON, Canada. [4]Department of Bioengineering, Stanford University, Stanford, CA, USA. [5]VA Palo Alto Healthcare System, Palo Alto, CA, USA. [6]Division of Cardiovascular Medicine, Stanford School of Medicine, Stanford, CA, USA. [7]Department of Cardiothoracic Surgery, Stanford School of Medicine, Stanford, CA, USA. [8]Department of Radiology, Stanford School of Medicine, Stanford, CA, USA. ✉e-mail: amarsden@stanford.edu

reduction in invasive catheterization procedures[23–25]. Patient-specific simulations have also shed light on biomechanical stimuli data, such as wall shear stress, that correlate with CAD progression and vein graft failure[26–32].

However, the accuracy of patient-specific coronary flow simulations depends on the quality of imaging upon which they are based. A common source of error is the exclusion of coronary arteries that are under-resolved by imaging. CFD models are often based on coronary computed tomography angiography (CCTA), which cannot accurately resolve vessels < 2 mm diameter[33]. Unsurprisingly, incomplete coronary artery branching in CFD models causes erroneous flow distributions amongst the arteries[34,35]. Simulated flow is also affected by the boundary conditions specified at each arterial outlet. A widely used method for prescribing these boundary conditions is Murray's law[36,37], which is an empirical relationship between the flow through an artery and its diameter. However, this method does not account for occluded and collateral arteries, microvascular dysfunction, and metabolic regulation. This method ignores inter-patient variability and is not personalized to each patient. As expected, this uncertainty in anatomy and boundary conditions significantly affects model predictions[38–44].

In this work, we propose a framework for increased personalization of coronary hemodynamics computational models that combines: (1) recent advances in clinical imaging of myocardial perfusion to obtain personalized coronary flow distributions; (2) computational methods to model vasculature beyond the limits of clinical imaging resolution; and (3) data-driven tools to personalize computational models by tuning parameters to match patient-specific clinical measurements. In addition, this framework reflects the multiscale nature of coronary circulation – including three dimensional flow in the large coronary arteries that can be reconstructed from CCTA, synthetic vascular trees for the small arteries that are under-resolved by CCTA, microvascular flow in the myocardial tissue, and closed-loop lumped parameter models for the heart and the systemic circulation.

In this framework, we personalize models to reproduce patient-specific coronary flow distributions by assimilating Dynamic CT Myocardial Perfusion Imaging (MPI_{CT}) into the CFD model parameters. MPI_{CT} is a CT-based non-invasive technique to quantify myocardial blood flow (MBF) distributions[11,12]. Imaging the coronary anatomy and MBF can be performed using a single CT imaging modality, and this has been used to diagnose CAD[16–18,45]. Since the myocardium is perfused by upstream coronary arteries, the myocardial flow distribution can be used to infer coronary flow distributions. This allows us to estimate personalized boundary conditions derived from MPI_{CT}, which are independent of purely empirical rules or vessel diameters[46].

Our framework also takes advantage of computational methods for generating realistic vascular trees[47]. This allows us to create more physiological coronary artery models by combining image-based anatomical models of epicardial vessels with synthetic vasculature for distal vessels. While similar approaches have been used previously[48–50], they have not incorporated high-fidelity flow simulations, closed-loop circulation models, or personalized boundary conditions. Here, we demonstrate a novel technique to tune such vascular trees, as well as the parameters of closed-loop lumped parameter circulatory networks, based on patient-specific measurements.

Finally, our hybrid image-based and synthetic vascular models of coronary flow are coupled to downstream models of microvascular flow in the myocardium[49–54]. Such models depend on several parameters, including properties of the tissue and flow in the upstream coronary artery tree. While previous studies have discussed the parameterization and estimation of tissue properties[53,55], they have not personalized the distribution of myocardial perfusion, which is dictated by the upstream coronary arteries. This work therefore seeks to recapitulate clinically measured myocardial perfusion using a multi-scale model of coronary flow.

The overarching aim of this work is to build accurate, personalized and multiscale computational models by assimilating clinical MPI_{CT} and cardiac function measurements. We emphasize that this framework does not aim to *predict* personalized hemodynamics in the absence of these clinical measurements. Instead, the goal is to assimilate clinical and imaging data into personalized model parameters such that the resulting models reflect the hemodynamics of each patient at the time of the clinical measurements. Such models provide a crucial baseline for performing virtual treatment planning based on clinical measurements of hemodynamics prior to treatment. We therefore describe the framework in the context of patient-specific data acquired prior to CABG surgery. This study represents an initial proof-of-concept to demonstrate the efficacy and utility of this personalization framework, which we apply on a cohort of six CAD patients. The objectives and novelty of this paper are hence as follows: (1) we demonstrate a personalized multi-scale computational simulation pipeline for coronary flow from the large blood vessels to the capillaries in the myocardium, which is informed by MPI_{CT}; (2) we demonstrate that parameter estimation can accurately recapitulate pre-treatment clinical measurements; (3) we compare hemodynamics of these personalized models with those constructed using conventional Murray's law-based boundary conditions and without synthetic vascular trees to highlight the importance of model personalization.

Results

We applied the framework developed in this work to personalize six patient-specific coronary hemodynamics models (Fig. 1). An overview of the framework is provided in Fig. 2. The framework starts with image-based anatomical models for the coronary arteries and the left ventricle (LV) that were reconstructed from CT angiography and MPI_{CT}. For each patient, we acquired myocardial blood flow (MBF) maps in the LV using MPI_{CT} (Fig. 2a, b). To estimate personalized vessel-specific coronary flows for each patient, we partitioned the LV into perfusion territories corresponding to each coronary artery (Fig. 2c) and computed the total MBF within each territory. We also augmented these image-based models with computationally-generated synthetic vascular trees to represent coronary vasculature below the resolution of the imaging and lumped parameter descriptions of systemic circulation, including the four heart chambers (Fig. 2d). This resulted in multiscale models of coronary circulation for each patient, which included three-dimensional image-based epicardial coronary arteries segmented from CCTA, synthetic vascular trees for smaller vessels,

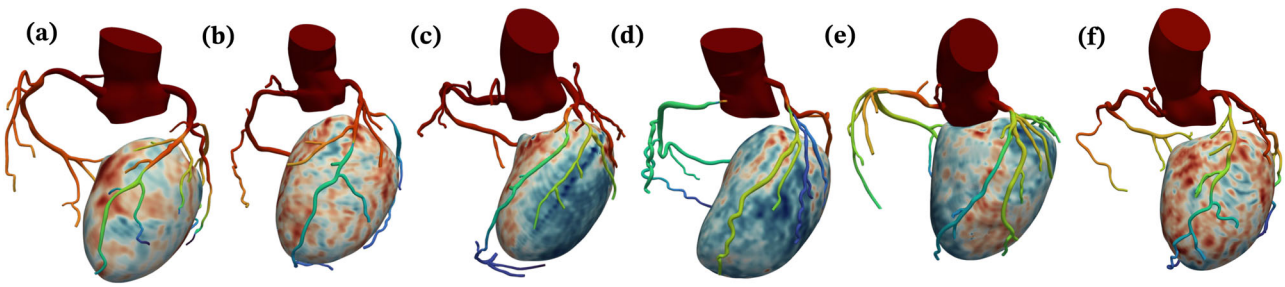

Fig. 1 | Coronary and LV anatomical models for the six patients in this study. The colors on the coronary arteries qualitatively represent simulated average pressure over a cardiac cycle and the colors on the LV represent MBF from MPI_{CT}. Figures **a**–**f** show patients 1–6, respectively.

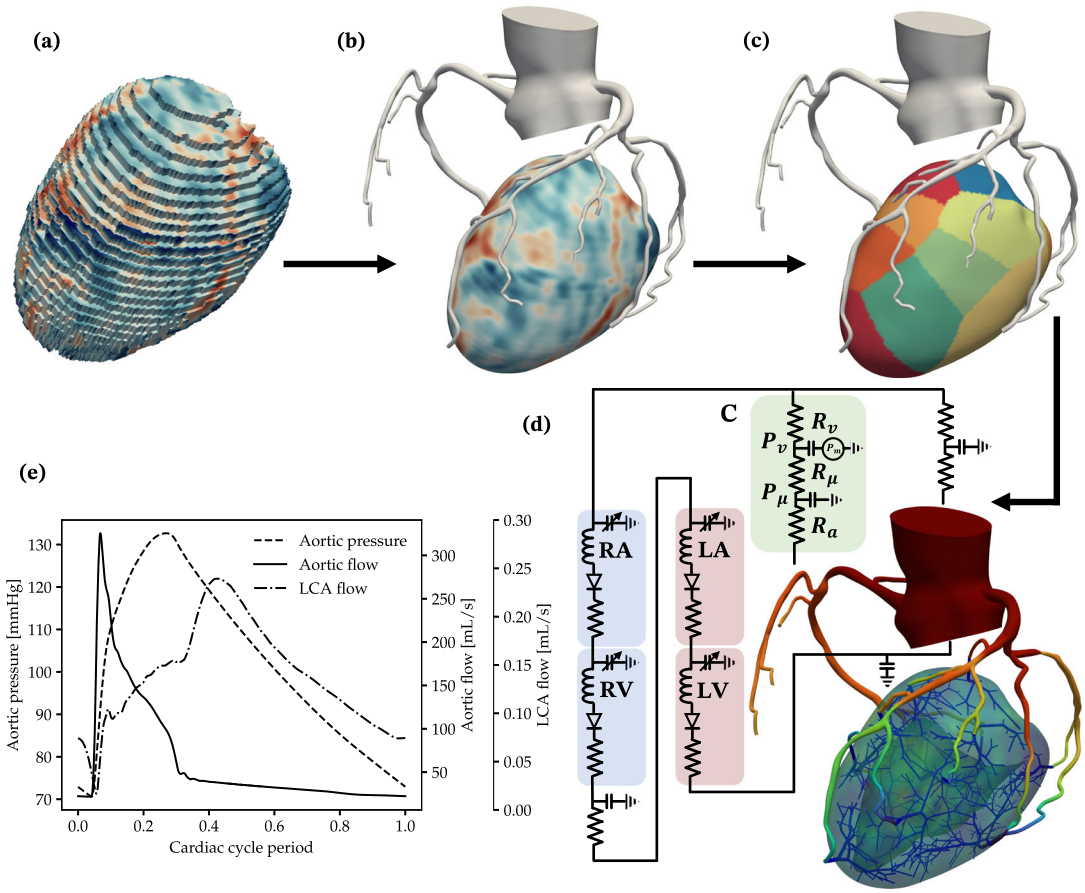

Fig. 2 | Overview of the computational modeling workflow. a Raw volume mesh of the LV, with color contours showing MBF from MPI_{CT}. **b** Segmented image-based coronary tree and the LV models after co-registration and processing. **c** LV perfusion volumes corresponding to each coronary artery. **d** The flow simulation setup, consisting of 3D models of the coronary arteries and LV, synthetic vascular trees perfusing the LV, and closed-loop boundary conditions. RA, RV, LA, LV and C denote the right atrium, right ventricle, left atrium, left ventricle, and coronary outlet LPN models respectively. **e** Simulated aortic pressure, aortic flow and left coronary flow over a cardiac cycle.

lumped parameter models for distal circulation, and Darcy models for flow in the myocardium (see sub-sections "Image-based modeling and coronary flow simulations," "Synthetic vascular trees," "Coronary flow boundary conditions," and "Myocardial blood flow simulations" of "Methods"). Computational simulations of blood flow were performed in the coronary vasculature and the LV using finite-element simulations. For each patient, we compared the hemodynamics resulting from models with and without synthetic vascular trees, as well as models that employed flow distributions based on patient-specific MPI_{CT} with the conventionally used Murray's law, which is based purely on vessel diameters. This resulted in a set of four models for each patient – with and without synthetic vasculature as well as with and without MPI_{CT}-informed flow distributions.

Each of these models was governed by several parameters that dictated the simulated cardiac function and coronary flow distributions. Model personalization was performed using a multi-stage optimization procedure. The first stage tuned the models to match patient-specific measurements of cardiac function and the second-stage tuned the models to match patient-specific flow distributions from MPI_{CT}. These flow distributions were computed in terms of the flow in each coronary artery, and for myocardial blood flow, they are reported within each region of the LV that is perfused by a specific coronary artery. In addition, the results are presented in terms of fractions of the total flow because MPI_{CT} is known to underestimate absolute flow[12].

The quality of the CCTA was lower for case 4 compared to the other cases, and this case was included to highlight the challenge posed by lower-quality clinical imaging. The imaging quality dictated the number of coronary artery branches that could be segmented for each anatomical model, resulting in 9 coronary artery branches perfusing the LV for case 4, and an average of 17 branches in the other cases. This section discusses the performance of the framework at recapitulating clinical measurements, as well as comparisons with boundary conditions based on Murray's law.

The performance of the first stage of the model personalization framework, which focused on estimating the parameters of the closed-loop LPN heart circulation model, is shown in Fig. 3. The framework successfully recapitulated patient-specific clinical targets, comprised of systolic/diastolic blood pressure and echocardiographic measurements of ejection fraction and ventricle volumes, for all 6 patients. The average error between the simulated and clinically measured targets was 5.07% for patient 1, 6.84% for patient 2, 4.36% for patient 3, 4.16% for patient 4, 3.88% for patient 5, and 5.35% for patient 6. The measured and computed values for these clinical targets are presented in Supplementary Table S1 of the Supplementary Information.

Our results reveal significant differences in the flow distributions within the coronary artery tree between models using Murray's law versus MPI_{CT}-informed boundary conditions. Figure 4 compares the simulated flow fraction at the outlet of each coronary artery with the corresponding flow fractions estimated from MPI_{CT} for each case without synthetic vascular trees. As expected for all cases informed by MPI_{CT}, there was reasonable agreement between the measured flow fractions from MPI_{CT} and simulated flow fractions. The mean error in flow fractions amongst all the coronary arteries in each case utilizing boundary conditions informed by MPI_{CT} was 8.85% for case 1, 11.06% for case 2, 10.80% for case 3, 21.04% for case 4, 2.05% for case 5, and 5.53% for case 6. We note that the low-quality imaging in case 4 posed an added challenge to the parameter estimation framework due to fewer coronary arteries perfusing the LV. Some arteries were therefore associated with unfeasible/unphysiological perfusion

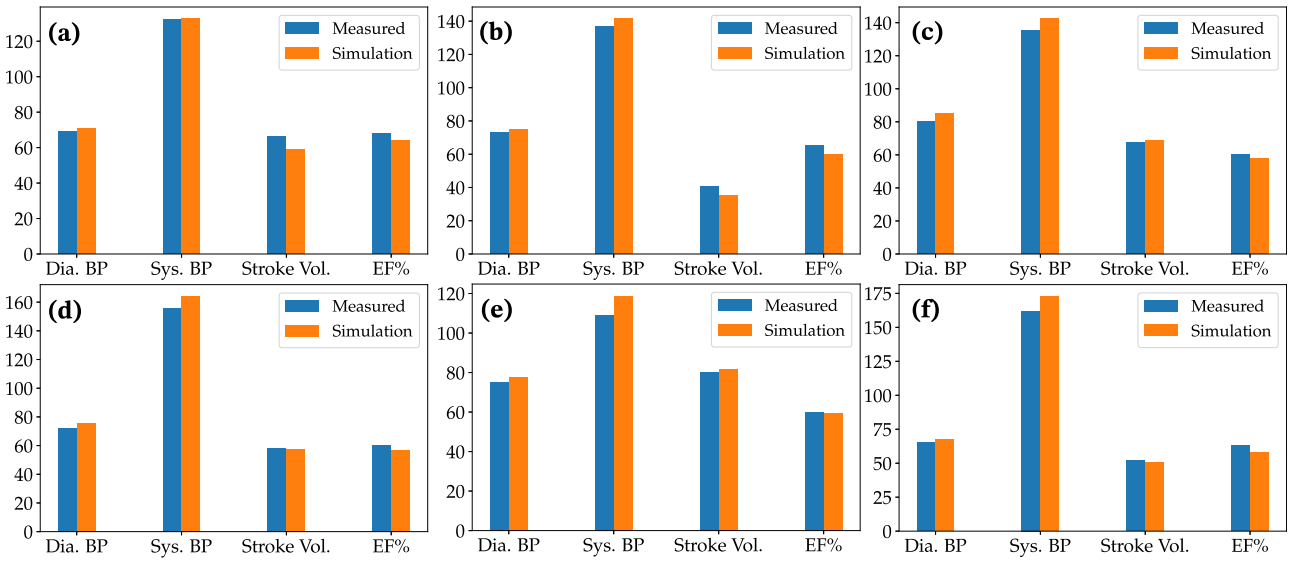

Fig. 3 | Comparison of simulated versus measured cardiac function for each patient. Figures **a**–**f** show data for patients 1–6, respectively. Dia. BP Diastolic blood pressure [mmHg], Sys. BP Systolic blood pressure [mmHg], Stroke vol. Stroke volume [mL], EF% Ejection fraction.

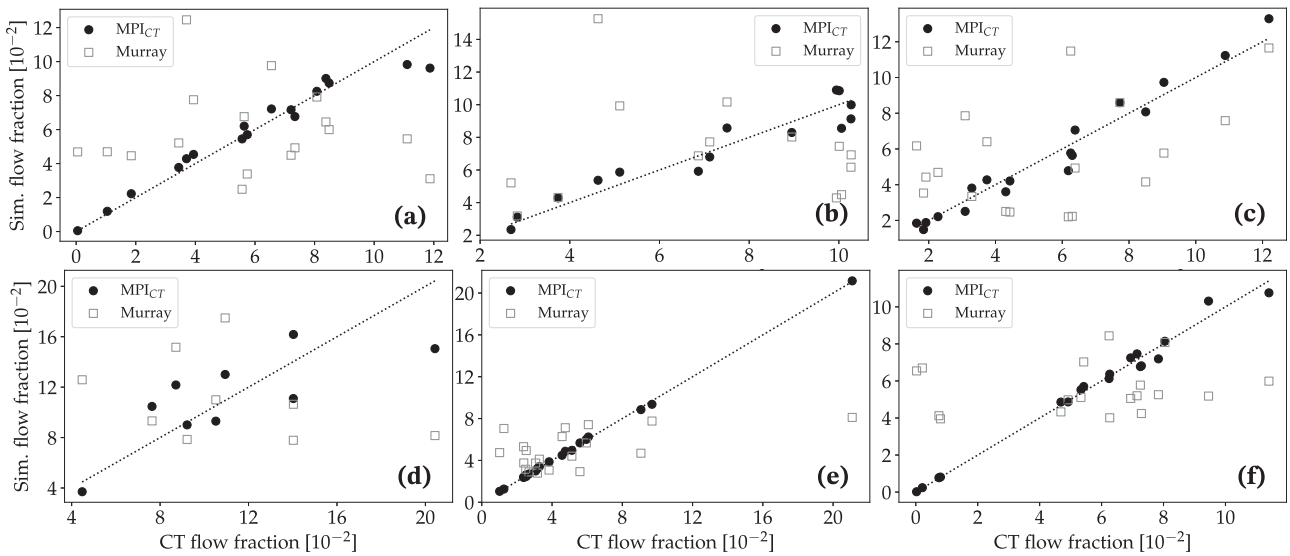

Fig. 4 | Comparison of simulated versus measured flow fraction in each coronary artery for cases without synthetic vascular trees. The simulated flow fractions are shown for cases using boundary conditions informed by MPI$_{CT}$ as well as Murray's law. Figures **a**–**f** show data for patients 1–6, respectively.

territories and flow fractions. Moreover, this case also included lesions at the ostium of the right coronary artery and other junctions between arteries, which were not captured in the 0D surrogate used for optimization (as is the case with most common 0D and 1D surrogate models). This is discussed further in section iii.

In contrast, the simulations utilizing boundary conditions based on Murray's law showed large deviations from the measured flow distributions. The mean error between the measured and simulated flow fractions amongst all the coronary arteries was 626.72% for case 1, 50.73% for case 2, 71.55% for case 3, 53.93% for case 4, 76.15% for case 5, and 1716.23% for case 6. By assessing the coronary artery branches in each case that showed the highest deviations from the measured flow distribution, we found that the branches with the largest errors were most often those affected by stenoses. However, there was no clear trend in the Murray's law boundary conditions either over- or under-estimating the flow in branches affected by lesions.

We also compared simulated MBF in the LV (section vi) against measured MPI$_{CT}$ on a branch-specific basis, i.e. the MBF within the regions of the LV associated with each coronary artery branch. Similar to the coronary flows, the simulated MBF distribution showed good agreement with MPI$_{CT}$ when using the framework developed in this work, and much larger deviations when using Murray's law-based boundary conditions (Fig. 5 without synthetic vascular trees). The mean territory-wise error in MBF fractions between MPI$_{CT}$ and simulations was 3.13% for case 1, 0.78% for case 2, 7.33% for case 3, 4.44% for case 4, 6.55% for case 5, and 1.34% for case 6. In comparison, boundary conditions based on Murray's law produced larger deviations of 17.88% for case 1, 11.32% for case 2, 26.71% for case 3, 17.45% for case 4, 28.06% for case 5, and 6.98% for case 6.

Similar trends were observed for the simulations with synthetic vascular trees. Figure 6 compares the simulated coronary flow fractions at all 500 synthetic tree outlets perfusing the LV with the flow distribution measured by MPI$_{CT}$ for all six cases. Similarly, Fig. 7 shows the simulated and measured MBF fractions in each vessel-specific LV perfusion territory. The mean error in flow fractions between the simulation and MPI$_{CT}$ was 14.48% for case 1, 12.68% for case 2, 20.32% for case 3, 23.45% for case 4, 19.76% for case 5, and 3.71% for case 6. In comparison, when using boundary conditions based on Murray's law the mean errors in flow

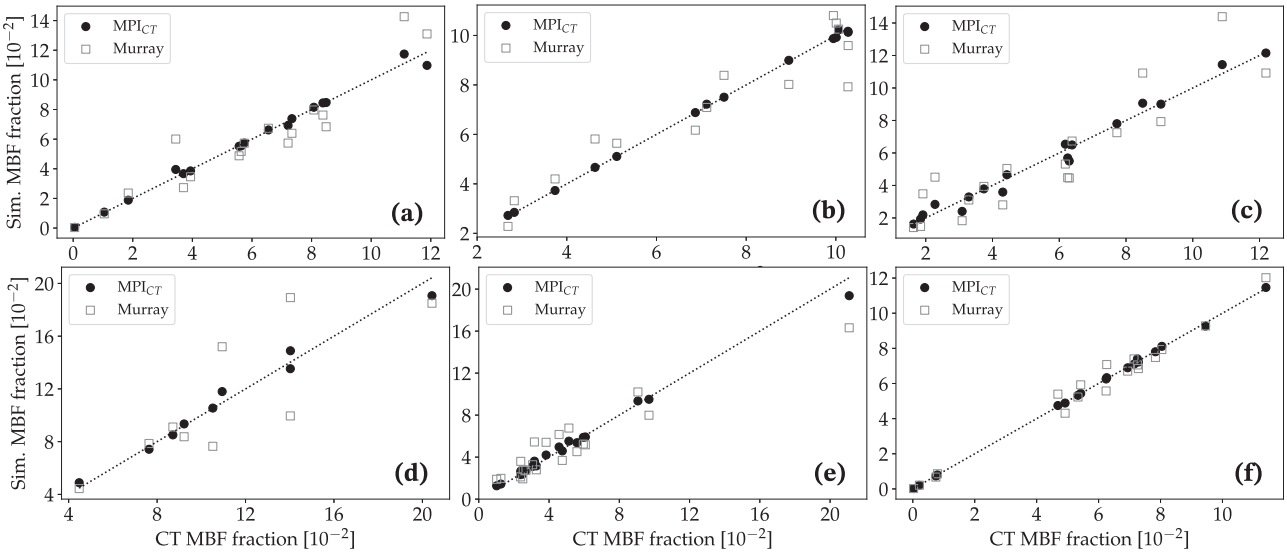

Fig. 5 | Comparison of simulated versus measured MBF fraction in each LV perfusion volume corresponding to a distinct coronary artery for cases without synthetic vascular trees. The simulated MBF fractions are shown for cases using boundary conditions informed by MPI$_{CT}$ as well as Murray's law. Figures **a**–**f** show data for patients 1–6, respectively.

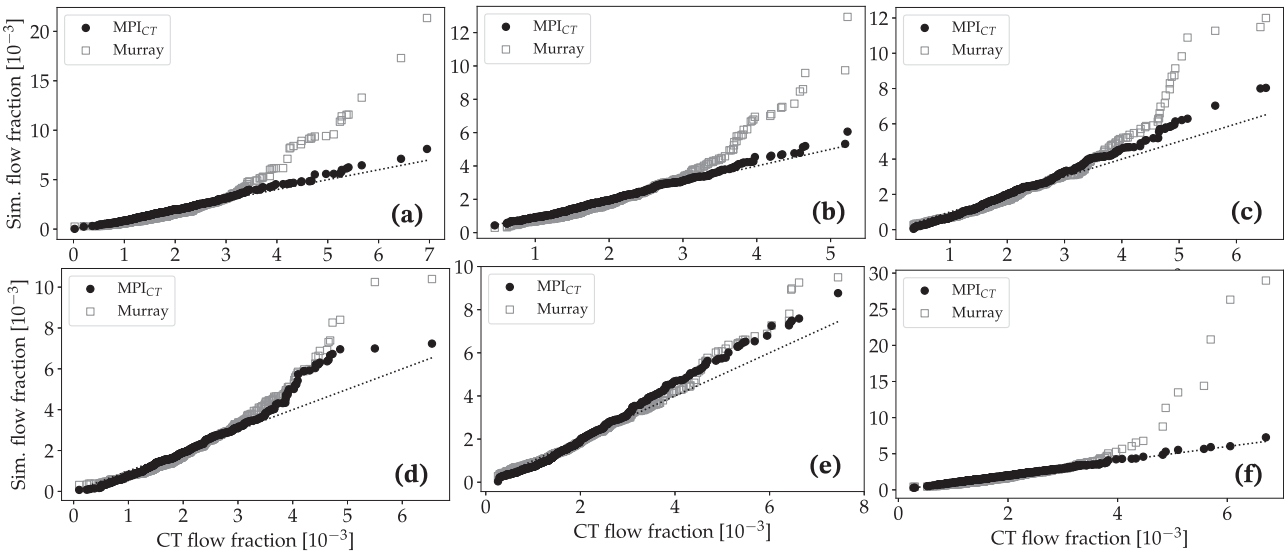

Fig. 6 | Comparison of simulated versus measured flow fraction in each coronary artery for cases with synthetic vascular trees. The simulated flow fractions are shown for cases using boundary conditions informed by MPI$_{CT}$ as well as Murray's law. Figures **a**–**f** show data for patients 1–6, respectively.

fractions were 130.45% for case 1, 79.77% for case 2, 79.97% for case 3, 98.98% for case 4, 110.22% for case 5, and 89.53% for case 6. The mean errors in MBF fraction when using MPI$_{CT}$-informed simulations were 4.50% for case 1, 2.23% for case 2, 7.28% for case 3, 6.25% for case 4, 7.57% for case 5, and 1.98% for case 6. These errors increased when using Murray's law to 21.04% for case 1, 14.30% for case 2, 32.83% for case 3, 24.29% for case 4, 32.24% for case 5, and 10.08% for case 6.

The utility of augmenting computational simulations with synthetic microvascular vascular trees to model physiological MBF distributions in the LV is highlighted in Fig. 8. Using case 1 as an example, Fig. 8a shows the clinically imaged MBF distribution on the LV from MPI$_{CT}$. This is compared with simulated MBF using synthetic vascular trees and Murray's law boundary conditions in Fig. 8b, MPI$_{CT}$-informed boundary conditions in Fig. 8c, and without synthetic vascular trees in Fig. 8d. It is evident that the MBF distribution obtained from the model with synthetic vascular trees and MPI$_{CT}$-informed boundary conditions best captured the clinically imaged MBF distribution, while the Murray's law-based simulation did not qualitatively agree with the clinical imaging. Although the simulation result without synthetic vascular trees (and with MPI$_{CT}$-informed boundary conditions) agreed well with clinically imaged MBF on a per-vessel basis (Fig. 5), the small number of vessels perfusing the LV led to an unphysiological MBF distribution on the LV (Fig. 8d). This illustrates the utility of the hybrid image-based and synthetic vascular models used in this work, particularly in the context of simulating physiological MBF distributions.

In current clinical practice, a widely used application of coronary hemodynamics simulations is the non-invasive estimation of FFR using CCTA-based anatomical models[22]. We therefore compared FFR along the main stenosed branches of each case computed from our simulations using boundary conditions based on Murray's law versus MPI$_{CT}$ flow distributions (Fig. 9). This was computed only in the epicardial image-based portion of each coronary artery where three-dimensional flow simulations were preformed, and is presented for models without synthetic vascular trees. For each vessel, we computed FFR at any given point along its length as the average pressure in the cross-section of the vessel at the given point divided

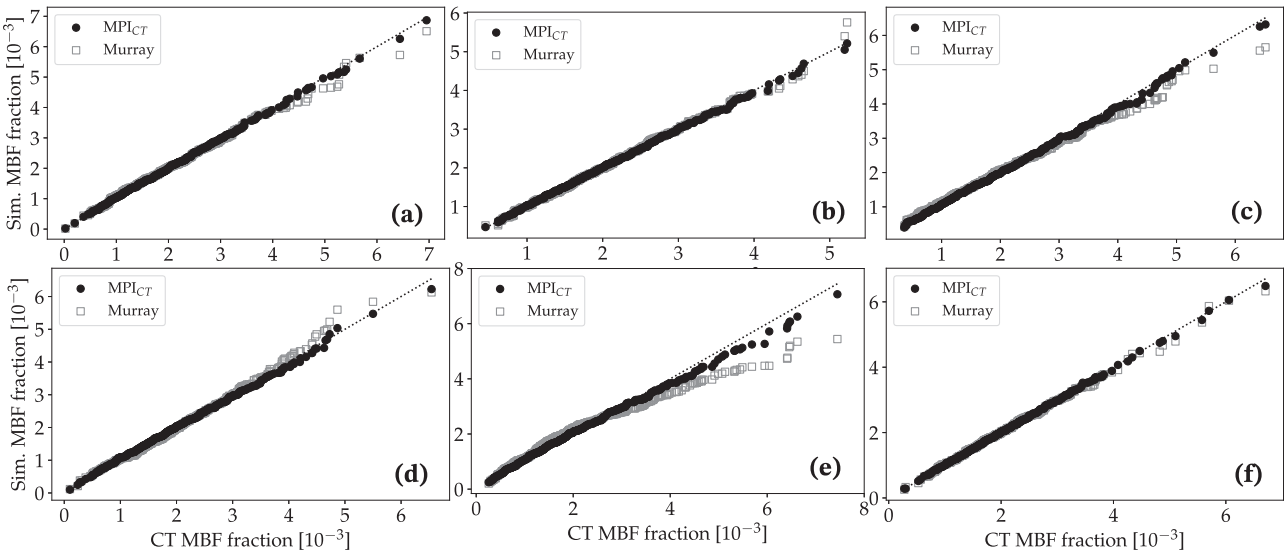

Fig. 7 | Comparison of simulated versus measured MBF fraction in each LV perfusion volume corresponding to a distinct coronary artery for cases with synthetic vascular trees. The simulated MBF fractions are shown for cases using boundary conditions informed by MPI$_{CT}$ as well as Murray's law. Figures **a**–**f** show data for patients 1–6, respectively.

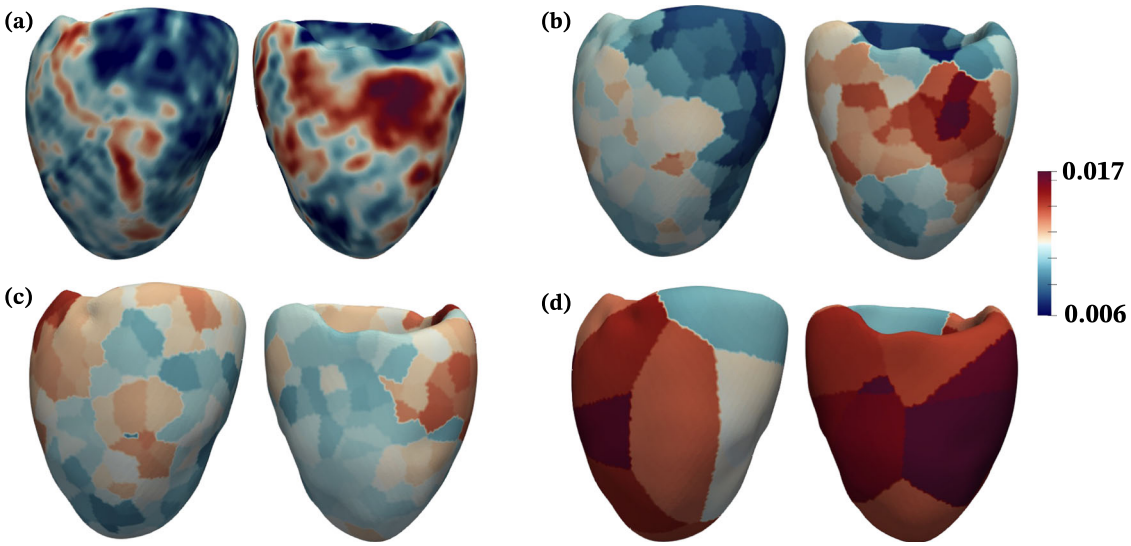

Fig. 8 | Comparison of the spatial distribution of MBF fraction on the LV for patient 1 from MPI$_{CT}$ and simulations. For each sub-figure, the posterior view is shown on the left and anterior view on the right. **a** MBF from MPI$_{CT}$. **b** MBF simulated using boundary conditions based on MPI$_{CT}$ and synthetic vascular trees. **c** MBF simulated using boundary conditions based on Murray's law and synthetic vascular trees. **d** MBF simulated using boundary conditions based on MPI$_{CT}$ without synthetic vascular trees.

by the aortic pressure. We observed that the difference in FFR computed using these two methods was vessel-dependent, with the RCA exhibiting substantial differences in cases 1, 2, 3 and 5. Differences were especially pronounced for case 1 (Fig. 9a), where the FFR computed using Murray's law was below clinically-used thresholds that signify ischemic risk (FFR < 0.80[14]) while the FFR computed using flow distributions from MPI$_{CT}$ was above this threshold. In this case, the RCA stenosis was approximately 50% based on invasive angiography and quantitative coronary angiography (QCA), however invasive FFR measurements were not available. This is also true, although to a smaller extent, for the RCA in cases 2 and 3 where the RCA, the LAD and diagonal branches in case 4, and the LAD in case 6, all of which had a 40%-60% intermediate-severity stenosis according to the angiographic readings and QCA. In comparison, both simulations based on MPI$_{CT}$ and Murray's law flow distributions produced FFR $\lesssim$ 0.80 for the circumflex and LAD in cases 1 and 2, the LAD in case 3, and the diagonal branch in case 4, all of which had stenoses in the range 60-70% or more, and/or diffused lesions, according to the angiographic readings and QCA.

Lastly, we compared the scaling of distal resistances at each coronary outlet obtained from the current MPI$_{CT}$-based framework with those prescribed according to Murray's law. This is shown for the left and right coronary artery trees for case 1 in Fig. 10a and b respectively, and for the left and right trees of case 2 in Fig. 10c and d respectively. We obtained a power-law fit between outlet resistance (R_o) and coronary artery diameter (d) given by $R_o \sim d^{-0.43}$ (R-squared = 0.17) and $R_o \sim d^{-0.78}$ (R-squared = 0.27) for the left and right coronary artery trees for case 1, and $R_o \sim d^{-0.23}$ (R-squared = 0.10) and $R_o \sim d^{-0.31}$ (R-squared = 0.13) for the left and right trees for case 2. It is evident that there is not a good power-law fit for the coronary artery diameter-flow relationship for these cases, and the obtained scaling differs significantly from the Murray's law relationship. This underscores the

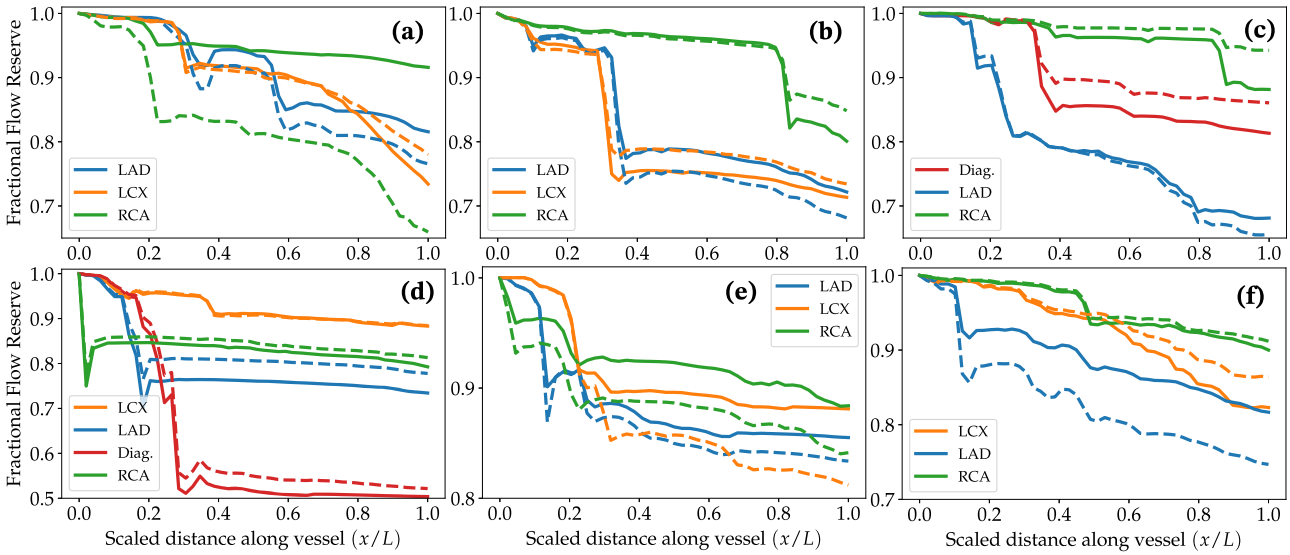

Fig. 9 | Simulated FFR using boundary conditions based on MPI_{CT} (solid lines) and Murray's law (dashed lines). a–f Show data for patients 1–6 respectively. For each vessel, the X-axis goes from 0 at the ostium to 1 at the outlet. LAD Left anterior descending artery, LCX Left circumflex artery, RCA Right coronary artery, Diag. Left diagonal artery.

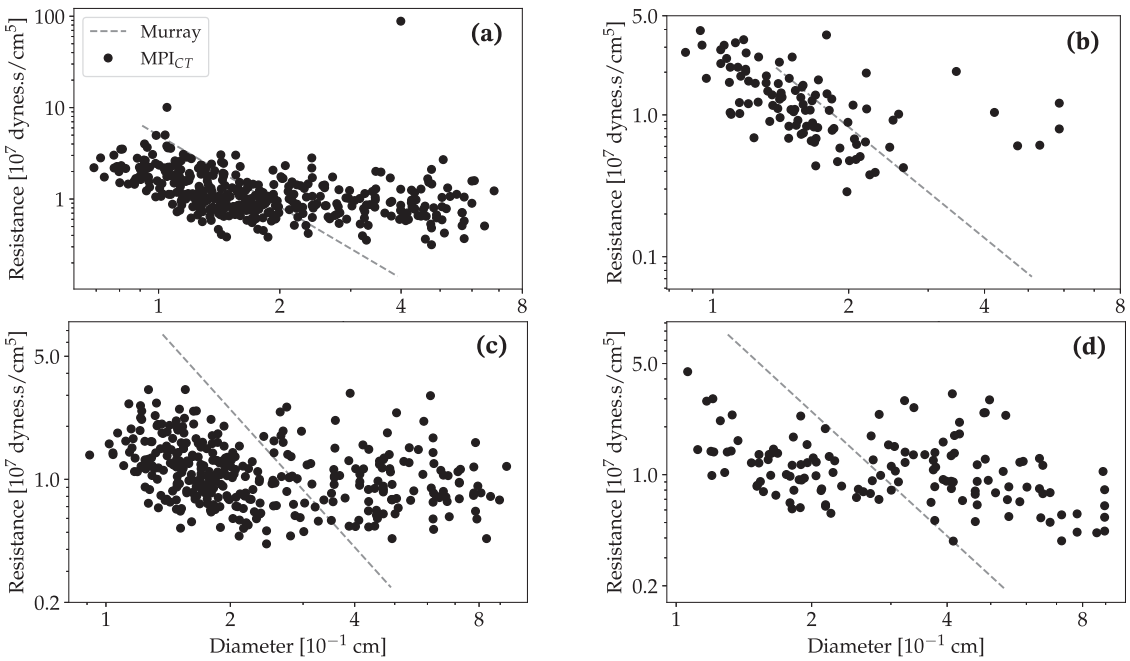

Fig. 10 | Diameter versus estimated resistance at outlets perfusing the LV based on MPI_{CT}. The dashed lines show the Murray's law scaling with exponent 2.6 for comparison. **a**, **b** Show the left and right coronary tree for patient 1, and **c**, **d** show the left and right coronary tree for patient 2.

inter-patient variability in coronary flow distributions and consequently, the need to incorporate novel clinical imaging such as MPI_{CT} to personalize computational models.

Discussion

We introduced an automated pipeline for personalizing computational models of coronary and myocardial blood flow informed by patient-specific clinical imaging and measurements. This study aimed to address two challenges in patient-specific coronary hemodynamics simulation models – the lack of patient-specific flow distributions in the coronary artery tree and inaccurate/incomplete branching patterns in image-based coronary artery anatomical models. To that end, we developed a simulation framework that includes the multiscale nature of coronary circulation from large epicardial vessels to myocardial microvasculature, and combined this with a novel parameter estimation procedure to yield personalized models. This represents a proof-of-concept for the incorporation of patient-specific clinical data, particularly MPI_{CT}, into novel multiscale coronary hemodynamics models. We note that our goal was not to predict personalized flow coronary flow a priori, but to demonstrate the potential value of improved model personalization by assimilation of novel imaging and clinical data into simulations. In the following discussion, we highlight the findings, limitations and future directions that stem from this work.

Impact of MPI_{CT}-informed coronary flow distributions

A major take-away from this study is that MPI_{CT}-based models resulted in significantly different flow distributions than Murray's law-based models.

The largest differences in coronary artery flow between models occurred distal to lesions. Moreover, our findings suggest that there is no consistent relationship across patients between the diameter of a coronary artery and its corresponding flow as measured by MPI_{CT}. With the caveat that this study was performed in a small cohort, this implies that the errors in coronary flow distribution arising from Murray's law based boundary conditions are not predictable a priori. However, this should be confirmed with larger patient cohorts and may differ in healthy patients, according to the work of van der Giessen et al.[38]. Crucially, the differences in flow within epicardial vessels between the models informed by MPI_{CT} and Murray's Law affected the computation of FFR, particularly in vessels with borderline lesions of ≈50% stenosis. Risk stratification based on hemodynamics is particularly valuable in these lesions[13,56], hence, the implications of these findings for the clinical use of computational models warrants more attention. A more detailed discussion of factors that must be considered prior to proving the clinical impact of these findings is provided in subsection iii below.

The difference in flow distributions resulting from Murray's law and MPI_{CT} likely stems from inter-patient variability arising from homeostatic vascular adaptation, coronary regulation, metabolic demand, etc., which are especially important in diseased coronary arteries and are not accounted for in Murray's law. Our findings agree with previous studies that have shown significant hemodynamic differences, especially in wall shear stress, between models that used boundary conditions based on Murray's law versus in vivo flow measurements[38,40,44]. We note, however, that these studies only included models of individual coronary arteries or single bifurcations, rather than the entire coronary artery tree simulated here.

Another reason for the inaccurate flow distributions resulting from Murray's law-based boundary conditions is its strong dependence on the outlet diameter of arteries. In the context of image-based computational models, these diameters are derived from segmentations that are error-prone. In contrast, one can view the use of MPI_{CT}-based boundary conditions as a lumped-parameter correction for inconsistencies that arise in the reconstruction of vessel lengths and lumen diameters in image-based models. For example, the resolution of clinical imaging dictates the length of each vessel visible in the image. However, this is not reflective of the actual length of the vessel, and its resultant hydrodynamic resistance or pressure drop. This therefore can be corrected for by optimizing lumped-parameter boundary condition resistances to compensate for inaccuracies in image-based segmentation. Indeed, as a demonstration of this, Supplementary Section S1 of the Supplementary Information provides results and discussion of the robustness of the MPI_{CT}-informed models versus those based on Murray's law in the context of segmentation variability for one patient in this study. In addition, recent work by Xue et al.[46], who demonstrated a framework to compute FFR from computational models informed by MPI_{CT}, also showed the robustness of such computational models to inaccuracies in segmenting coronary epicardial vessels.

In the context of clinical translation, a particular advantage of MPI_{CT}-informed models is the ability to provide high-resolution, full coverage quantification of MBF. The ability to resolve vessel-specific MBF distributions (in contrast to lower-resolution perfusion imaging methods such as PET/SPECT) is especially valuable in the context of the framework demonstrated here. Moreover, there are clear advantages to using a single imaging modality to produce both CCTA and MPI_{CT} so that the entire framework can be integrated into a single non-invasive imaging protocol. The prognostic value of MPI_{CT} for detection of functionally significant CAD was previously demonstrated in several studies[16–18,45], and its incorporation into computational models has substantial potential for added clinical value.

Synthetic vascular trees and multi-scale modeling

Another contribution of this work is the incorporation of the automated model personalization with multi-scale models of coronary hemodyamics. Our framework included flow in vessels smaller than the CCTA imaging resolution, microvascular perfusion in the myocardium, and LPN models of cardiac function and systemic circulation.

Our use of synthetic vascular trees appended to image-based coronary vessels is motivated by studies that have highlighted the effect of inaccurate coronary artery branching on modeled hemodynamics[34,35]. Synthetic vascular trees provide a viable method to address this challenge even when using imaging of insufficient resolution, especially when combined with published morphometric data[57] to create realistic vascular anatomies. Moreover, we demonstrated that models of myocardial perfusion that include more uniform and realistic vasculature can more accurately recapitulate clinically imaged MBF distributions. This also translates to the assimilation of data from MPI_{CT} data into computational models, i.e. higher resolution coverage of the perfusion volume by synthetic vasculature allows higher-fidelity assimilation of MPI_{CT} data into computational models. Finally, another motivation for this approach is to enable the modeling of physiological vascular adaptation resulting from treatments. As stated previously, an ultimate goal of developing this method is to use models tuned to patient-specific pre-treatment measurements for the prediction of post-treatment outcomes. To achieve this, it is important to model homeostatic vascular adaptation following treatments, which can be performed more accurately within individual vessels by using these vessel-scale models of distal vasculature rather than purely lumped-parameter descriptions[58].

Furthermore, our incorporation of closed-loop LPN models representing cardiac function allows us to further personalize models based on clinical measurements, rather than using literature-based boundary conditions. Such LPN models have been previously used for model-based treatment planning and to model patient-specific changes in cardiac function[59]. In addition, the coupling of the upstream hemodynamics in the coronary artery tree with the microvascular blood flow in the myocardium could enable models of coronary revascularizaton on myocardial tissue. This is infeasible in prior models of coronary hemodynamics that focus exclusively on epicardial hemodynamics[22]. Finally, this multi-scale framework opens up the possibility of studying microvascular disease using computational models. A recently proposed metric, Microvascular Resistance Reserve (MRR)[60], has been shown to provide improved clinical diagnosis in patients where existing epicardial disease is a confounding factor in the assessment of microvascular disease. However, the non-invasive estimation of MRR depends on being able to model coronary microvasculature and also accurately estimate patient-specific coronary flows non-invasively – both of which this framework can potentially be used for.

Limitations and future work

We recognize several limitations in this study. We first emphasize that this study was performed on a small cohort of six patients to demonstrate the added value of incorporating MPI_{CT} into multiscale models of coronary flow. This is therefore a proof-of-concept, and further work is required to establish clinical relevance. Most importantly, this framework needs to be tested on larger patient cohorts and correlated with clinical outcomes. We also did not explore the use of this method in coronary artery pathologies other than CAD. Below, we highlight several other factors that should be considered in future work.

The framework presented was deterministic, utilizing single measurements of the clinical targets for each patient to optimize the computational models. However, each clinical measurement is associated with various sources of uncertainty from the measurement protocols, patient physiology, as well as post-processing. In addition, the model can include anatomical uncertainty stemming from segmentation as well as the generation of synthetic vascular trees. Future work should account for uncertainties in the estimation of patient-specific parameters as well as in the model predictions; this can be performed following recent work in uncertainty quantification by our group and others[43,61–63]. Similarly, the sensitivity of the model to different parameters also needs to be assessed. Additionally, the dataset used here did not include clinically measured intra-coronary flow to compare with the estimated flows from MPI_{CT}. While the goal is to build a non-invasive framework based entirely on MPI_{CT}, comparisons with intra-coronary measurements would be valuable to increase confidence.

Table 1 | Summary of patient data

Patient	BP (mmHg)	SV (mL)	LVEF	LAD stenosis	LCX stenosis	Diag. stenosis	RCA stenosis
1	132/69	66.3	0.68	65% diffuse	65% proximal	N.A.	50% proximal
2	137/73	40.4	0.65	65% medial	70% proximal	N.A.	55% distal
3	135/80	67.2	0.60	55% diffuse	N.A.	55% proximal	45% distal
4	156/72	58.4	0.60	50% proximal	45% med.	70% proximal	75% proximal
5	109/75	80.4	0.60	40% proximal	35% diffuse	N.A.	40% proximal
6	162/65	52.1	0.63	50% proximal	<30%	N.A.	50% medial

The stenosis are reported as percentage diameter stenosis.
BP Systolic/diastolic blood pressure, *SV* Stroke volume, *LVEF* LV ejection fraction, *LAD* Left anterior descending artery, *LCX* Left circumflex artery, *Diag* Diagonal branch, *RCA* Right coronary artery.

Another area for improvement is the complexity of the modeling utilized. While we used 3D simulations of coronary hemodynamics to compute FFR, the parameter estimation used 0D surrogate models that deviated from the true hemodynamics. In particular, 0D models do not accurately capture the flow within stenoses and at junctions between arteries. This contributed to larger errors in the flow distributions predicted from 3D models than the thresholds specified in the surrogate-based parameter estimation. Improved surrogate models will also be valuable for applying this method within time-frames that are feasible for clinical use. Another simplification was the single-compartment Darcy model we used to simulate myocardial perfusion and the one-way coupling between upstream coronary flow and myocardial blood flow. Previous work[53] has shown heterogeneity and anisotropy in the myocardial microvasculature, which are ignored by the assumption of constant, isotropic permeability. This also does not account for pathologically altered myocardial microvasculature and tissue, which can occur in the case of infarction in CAD patients. In fact, this is not only a challenge in the computational model, but the accurate estimation of MBF from MPI_{CT} is an additional challenge in that context due to the resulting reduction in left ventricular wall thickness. Future work should incorporate heterogeneity in the myocardial tissue properties that reflects both healthy and diseased tissue. This should also consider growth and remodeling of microvasculature in response to normal and pathological hemodynamics[64]. The two-way coupling between the myocardial blood flow and upstream coronary flow, as in ref. 49, should also be considered. Moreover, the permeability was not tuned to patient-specific measurements.

This framework would also benefit from a more physiological partitioning of the myocardium into regions perfused by each coronary artery. Although there is evidence that each part of the coronary artery tree perfuses a distinct volume of the myocardium[52,65], there is no consensus method to perform this partitioning in previous studies[40,46,49,54]. However, these perfusion regions affect the simulated flow through each coronary artery. They also influence the structure of the synthetic vascular trees that extend into the myocardium from epicardial coronary arteries. While we generated vascular trees within pre-defined LV perfusion regions, future work will include methods to grow larger synthetic vascular trees that compete to perfuse physiological regions of the myocardium. We also note that the method proposed here does not depend on the particular choice of myocardial perfusion region corresponding to each artery, because the main input to the framework is simply the resulting vessel-specific flow. Supplementary Section S2 of the Supplementary Information demonstrates this for one sample case where the perfusion territories were computed based on the entire lumen for each artery, which is a common alternative to the method used here based on just the coronary outlets.

As mentioned earlier, the main goal of this work was to develop models for personalized CAD treatment planning. To that end, future work will explore applying these tools to predict the hemodynamics of patients after CABG surgery. This will involve studies in larger patient cohorts and methods to account for post-surgical vascular and cardiac adaptation.

Conclusions

We introduced an automated pipeline for personalized and realistic computational models of coronary and myocardial blood flow informed by patient-specific clinical imaging and measurements. We used image-based coronary artery anatomical models augmented with synthetic vascular trees to create patient-specific anatomical models with more realistic branching. We personalized these models using flow distributions informed by MPI_{CT} and measurements of cardiac function by ultrasound. The simulation framework included three-dimensional simulations of blood flow in the coronary arteries and the left ventricle, coupled with closed-loop LPN models of distal and systemic circulation. We showed that our simulation framework was successfully able to assimilate and recapitulate the clinical measurements. These personalized models produced significantly different results from those based on conventionally used boundary conditions. This has important implications for the non-invasive computation of clinically-relevant metrics, such as FFR and MBF, from CFD simulations.

Methods

Patient population

We performed simulations on a subset of six patients (Fig. 1) from a cohort who were scheduled to undergo coronary artery bypass graft (CABG) surgery, and also underwent coronary CT angiography (CCTA) and dynamic CT myocardial perfusion (MPI_{CT}) imaging at Stanford University School of Medicine, Stanford CA, USA as part of an ongoing study (NCT03894423). This study was approved by the Institutional Review Board at Stanford University School of Medicine. Written informed consent was received prior to patient participation. The exclusion criteria for the cardiac CT exam were: (1) Age < 40 years; (2) left ventricular ejection fraction < 30%; (3) repeat CABG; (4) contra-indications to iodine contrast medium, including eGFR < 45 ml/min, known contrast allergy; (5) contra-indications to vasodilators, including bronchial asthma, advanced atrioventricular block, sinus node disease, clinically significant carotid artery narrowing, severe aortic stenosis or left ventricle outflow tract narrowing, blood pressure < 90mmHg, use of dipyridamole or aminophylline; (6) conditions technically challenging the examination, including severe valvular disease, atrial fibrillation and body weight > 100 kg; (7) other conditions of that would render the examination unsafe, including pregnancy, unstable ischemia, severe arrhythmia, heart failure. From the patient cohort that underwent a cardiac CT exam, the inclusion criteria for this computational modeling study were the availability of CCTA and MPI_{CT} images of sufficient quality to re-construct the 3D coronary anatomy and myocardial blood flow (MBF), as well as clinical measurements of heart rate, blood pressure, cardiac output and ejection fraction measured at the time of the CCTA. None of the patients in the cohort included in this study had previous stents or in-stent restenosis. A summary of the patient data and angiographic readings are provided in Table 1.

Clinical imaging protocols and processing

MPI_{CT} followed by CCTA were performed on a third-generation dual-source CT scanner (SOMATOM Force, Siemens Healthineers). Hyperemia was induced by slow bolus injection of 0.4 mg regadenoson. A 40-ml bolus

of iopamidol (Isovue, 370 mg/ml, Bracco, Italy) was injected at 5.5 ml/s followed by 40 ml saline. The dynamic perfusion protocol requires that the table position is repeatedly alternated (shuttle mode) to completely cover the myocardium and acquire up to 15 data samples during a 30 s breath hold. Acquisition parameters were 80-kV tube voltage, automated exposure control (300 mAs/rotation at 80 kV as reference), 96 × 0.6-mm detector collimation, 105-mm z-axis coverage, 250-ms gantry rotation time, and 66-ms temporal resolution. Reconstructed images with a 3.0-mm slice thickness, and 2.0-mm reconstruction interval were processed on a dedicated workstation (Syngo.CT Myocardial Perfusion, Siemens Healthineers). Serial samples were aligned using a motion correction algorithm. The arterial input function was sampled in the descending aorta. Time-attenuation curves were created for each voxel within the segmented left ventricle (LV) myocardium. Using a dedicated parametric deconvolution algorithm based on a 2-compartment model of intra- and extravascular space, a fit curve was created. MBF was calculated as the ratio between the maximum slope of the fit curve and the peak arterial input function, and the results were exported as three-dimensional MBF maps (Fig. 2a). Comprehensive descriptions of the myocardial perfusion protocol and the calculation of MBF can be found in[66].

A standard CCTA was performed 10 min after MPI_{CT} by prospective ECG-triggered axial scan mode. The tube voltage ranged between 100 and 120 kV and the spatial resolution was approximately 0.5 mm in all three dimensions. Most patients received 50 mg aminophylline after the perfusion scan, as well as intravenous metoprolol if the heart rate exceeded 70 bpm. All patients received sublingual nitroglycerin just before the contrast-enhanced CT exam.

Since the CCTA and MPI_{CT} were performed at mid-diastole and systole respectively, they were co-registered using the affine registration procedure implemented in *3D Slicer* (www.slicer.org). The LV myocardial volume was then segmented from the co-registered MPI_{CT} image using thresholding in *ParaView* (www.paraview.org). It was smoothed and meshed with tetrahedral elements using *Meshmixer* (www.meshmixer.com) and *TetGen*[67], respectively. Finally, the MBF values at each voxel of the MPI_{CT} scan were interpolated on to the nodes of the LV mesh, making sure the total MBF was equal between the two. Note that all the software used for the processing of these images are freely available, and all except *Meshmixer* are open-source. Figure 2b shows the 3D volumes of the co-registered LV and coronary vasculature for patient 1.

Following the construction of co-registered 3D models of the LV myocardium and coronary arteries, the LV volume was divided into non-overlapping sub-volumes corresponding to the perfusion territory of each coronary artery (Fig. 2c). This was done using Voronoi tessellation, where each node in the tetrahedral mesh for the LV volume was assigned to its closest coronary artery outlet. Therefore, each coronary artery outlet was associated with a distinct region of the LV myocardium. Subsequently, the flow-rate associated with each coronary outlet was estimated by integrating the MBF obtained from MPI_{CT} within each corresponding LV perfusion territory. This resulted in the total flow into the LV territory associated with each coronary artery. In addition, the units of MBF, which were expressed in mL/min/100mL in the clinical measurements, were converted to units of mL/s for consistency with flow-rate units in the computational models. We note that the LV perfusion territories corresponding to each coronary artery can also be computed based on the distance of each point in the LV to the closest coronary artery (instead of coronary artery outlet)[40,46] as well as weighted measures of distance[49,54]. This approach was chosen for simplicity, however, the framework presented in this work is equally applicable to any method for computing perfusion regions in the LV. In fact, we have applied the framework to one case, which is discussed in Supplementary Section S2 of the Supplementary Information, where the LV perfusion territories were computed based on the distance of each point in the LV to the closest coronary artery, rather than just the outlet. The framework worked as expected and was able to recapitulate clinical measurements for the patient.

Image-based modeling and coronary flow simulations

We used the open-source *SimVascular* software[68] for segmentation of coronary arteries from CT angiography images, construction of 3D anatomical models, and coronary flow simulations. The segmentations were performed manually from CT angiography and were informed by quantitative coronary angiography. They were performed by the first author (K.M.) and supervised by an expert in CT-based cardiac imaging (K.N.). Tetrahedral finite element meshes were created using the open-source *TetGen* package[67], which is included with *SimVascular*. Three dimensional flow simulations were performed using the *svSolver* flow solver within *SimVascular*, which uses a stabilized finite element method with linear tetrahedral elements for spatial discretization and generalized-α time-stepping with second-order time accuracy[69,70].

The governing equations for coronary blood flow were the three-dimesional incompressible Navier-Stokes equations,

$$\nabla \cdot \vec{u} = 0; \rho \frac{\partial \vec{u}}{\partial t} + \rho \vec{u} \cdot \nabla \vec{u} = -\nabla p + \nabla \cdot (\mu \nabla \vec{u}) \quad (1)$$

where $\vec{u}$ and p are the blood flow velocity and pressure, respectively. Blood was assumed to be a Newtonian fluid with viscosity $\mu = 0.04$ dynes/cm^2 and density $\rho = 1.06$ g/cm^3. The Newtonian fluid assumption is valid because non-Newtonian effects begin to be apparent only for blood vessels with diameters below 300 μm[71], which was approximately the limit of the smallest vessels modeled in this study.

Coronary artery walls were treated as deformable, and fluid-structure interaction arising from the coupling between blood flow and the artery walls was handled using the coupled momentum method[72]. Material properties for the artery walls were selected based on literature data following previous work[73,74]. The elastic modulus for the aorta and coronary arteries were set to 0.25 MPa and 1.15 MPa, respectively[75–77]. Wall thicknesses were based on published radius-thickness ratios for the aorta[76] and morphometric data for the coronary arteries[78]. Mesh convergence for the tetrahedral meshes were established in a recent study using a similar coronary hemodynamics modeling setup[74].

Synthetic vascular trees

We augmented our image-based coronary artery anatomical models with synthetic vascular trees to model coronary vasculature with diameters below the imaging resolution of the CCTA. Constrained Constructive Optimization (CCO)[47] was used to generate synthetic vascular trees that are constrained by vascular scaling laws and hemodynamic factors while minimizing vascular volume. CCO has recently been adapted to generate multiple non-intersecting trees within non-convex ventricle-like tissue volumes[48], although this process is computationally expensive. In this work we used an improved open-source implementation of Sexton et al.[79] to more efficiently generate synthetic vascular trees at the outlet of each coronary artery that perfused the LV. While the CCO implementation used here allows the generation of several competing vascular trees within the same tissue volume, we chose to generate one independent vascular tree within the LV volume associated with each coronary artery. In our experience, this approach resulted in the LV being more uniformly vascularized and with significantly lower computational cost by avoiding the generation of unphysiological competing tree morphologies from approximately 15 coronary artery outlets.

For each case simulated in this work, we generated synthetic vasculature with a total of 500 outlet branches perfusing the LV (compared to approx. 16 branches perfusing the LV in the purely image-based anatomical models). The total number of synthetic outlet branches was divided amongst the vascular trees appended to each coronary artery outlet based on the size of their corresponding LV perfusion volumes. The smallest vessels produced were approximately 300 μm in diameter. Flow in the synthetic vasculature was modeled using a lumped-parameter/0D representation of the vessels, which included resistance, capacitance and inductance to model viscous losses, wall dilation, and fluid inertia respectively. The lumped-

parameter resistance, capacitance and inductance of each vessel were given by linearization and Poiseuille flow simplifications of the Navier Stokes equations[80]. The lumped-parameter flow in these synthetic vascular trees was simulated using the open-source *svZeroDPlus* solver, which is part of the *SimVascular* software suite, and was coupled to the hemodynamics in the 3D image-based anatomical model using a modular implicit coupling method[81].

Coronary flow boundary conditions

We used a closed-loop lumped parameter network (LPN) model to enforce boundary conditions for the coronary flow simulations at the aortic inlet and the aortic and coronary outlets of the 3D model[74,82,83] (Fig. 2d). The LPN included specific features to model distal systemic resistances using Windkessel models[84] and the effect of the four heart chambers. It also captured the distal resistance and intra-myocardial pressure experienced by coronary arteries, which produces out-of-phase coronary flow with respect to the cardiac cycle[85]. Figure 2e shows representative pressure and flow waveforms for one case. As seen in Fig. 2(d), the LPN boundary conditions at the coronary artery outlets consisted of three resistance elements – R_a, R_μ and R_v – to model the resistance of small arteries, microvasculature, and the venous system, respectively. The values of total resistance ($R_a + R_\mu + R_v$) distal to each coronary artery determined the distribution of flow amongst the arteries in the coronary artery tree. These resistance and capacitance elements distal to each coronary artery in the model, as well as other parameters of the LPN, such as the elastance and capacitance of each heart chamber, the systemic vascular resistances, etc. were tuned to match clinically measured metrics of cardiac function and coronary flow distributions for each patient (see section vii). As with the lumped parameter representation of the synthetic vascular trees discussed in section iv, the closed-loop LPN boundary conditions were simulated using *svZeroDPlus* and coupled with the 3D flow solver using a modular implicit coupling method[86].

We also simulated coronary flow at hyperemia to recapitulate common clinical measurements that assess coronary hemodynamics under stress (including FFR and MPI_{CT}). We simulated hyperemia by scaling the resistance boundary conditions distal to coronary arteries by a factor of 0.24 compared to baseline resting values[87], as commonly done in FFR_{CT}[22].

Myocardial blood flow simulations

Myocardial perfusion in the arterioles and capillaries within the LV myocardium was modeled as flow through a porous material due to the prohibitive computational cost of resolving discrete microvascular blood vessels[49–54]. Flow through porous materials is described by Darcy's Law, and in this work we used a single-compartment Darcy model governed by the equations,

$$\vec{w} + \boldsymbol{K}\nabla p = 0; \nabla \cdot \vec{w} = \beta_{psrc}(p_{src} - p) - \beta_{snk}(p - p_{snk}), \qquad (2)$$

where $\vec{w}$ and p are the Darcy flow velocity and pressure, respectively. The permeability of the LV myocardial tissue is given by $\boldsymbol{K}$. We assumed constant and isotropic permeability for simplicity, as in prior Darcy models for myocardial perfusion[49,51,54,55], i.e. $\boldsymbol{K}(\vec{x}) = k\boldsymbol{I}$, where $\boldsymbol{I}$ is the identity tensor and k is the scalar, spatially-constant permeability. We fixed $k = 2 \times 10^{-5}$ cm^2 Pa^{-1} s^{-1}, which is informed by previous work[49,51]. Myocardial perfusion was driven by the coronary flow in the upstream vasculature via pressure source terms, which are denoted by p_{src} in Eq. (2). These pressure sources, corresponding to the outlet of each coronary artery that is perfusing the LV, were specified as the microvascular pressure in the coronary outlet boundary condition model (see section v and P_μ in Fig. 2d). Therefore, each perfusion territory associated with a coronary artery outlet, discussed in section ii, was assigned a corresponding spatially distributed pressure source. Moreover, the coupling between the upstream coronary flow and myocardial blood flow is one-way. The pressure of the venous return system is given by p_{snk} in Eq. (2), and represents a sink for myocardial perfusion. We assumed $p_{snk} = 0$ mmHg in this work[49]. Lastly, the terms β_{src} and β_{snk} represent the conductance of flow entering and leaving the tissue, respectively, and were parameterized as follows,

$$\beta_{src} = \frac{Q_{LV}}{V_{LV}(\bar{p}_{src} - p_{cap})}; \beta_{snk} = \frac{Q_{LV}}{V_{LV}(p_{cap} - p_{snk})}. \qquad (3)$$

In Eq. (3), Q_{LV} and V_{LV} are the total flow perfusing the LV and the volume of the LV respectively. The spatially-averaged pressure source (p_{src}) is denoted as $\bar{p}_{src}$ and p_{cap} is the target capillary pressure assumed to be $p_{cap} = 15$ mmHg[49,51]. Note that for a given tissue volume $V_i \subseteq V_{LV}$, such as one vessel-specific perfusion territory, the MBF within that volume is given by,

$$MBF_{V_i} = \int_{V_i} \beta_{psrc}(p_{src} - p)dv. \qquad (4)$$

We simulated perfusion in patient-specific LV volumes segmented from MPI_{CT}, as described in section ii. Unstructured tetrahedral meshes were generated using the open-source *TetGen* package[67], and pressure sources (p_{src}) were imposed from flow simulations in the coronary arteries for each patient-specific case. A finite element solver for Eq. (2) employing linear tetrahedral elements was implemented in the open-source *svFSI* software, which is part of the *SimVascular* software suite. We used zero-flux boundary conditions on the surface of the LV mesh and iterated the steady state problem to convergence. We note that while the Darcy model was simulated on the entire LV mesh, we present the results in terms of MBF, which as shown in Eq. (4) above, is integrated over each vessel-specific perfusion territory. While the solution for p in Eq. (2) is itself a smooth field, the results presented int erms of MBF (as in Fig. 8) are not smooth because p_{src} is not smooth and depends on each vessel-specific perfusion territory.

Parameter estimation for personalized boundary conditions

We employed a multi-stage surrogate-based optimization procedure to estimate the parameters of the closed-loop LPN boundary condition model (discussed in section v) to recapitulate measured clinical data for each patient. This was performed for purely image-based models as well as those augmented with synthetic vascular trees. The clinical targets we used were the vessel-specific flows from MPI_{CT}; systolic and diastolic aortic pressure from blood pressure cuff measurements; left ventricular ejection fraction, stroke volume, cardiac output and systolic/diastolic ventricular volumes from echocardiography; and physiological targets derived from literature including pulmonary pressure and coronary flow waveforms[83,88,89]. While the vessel-specific flows from MPI_{CT} were measured at hyperemia, the other clinical targets were measured at rest. This was accounted for in the tuning procedures detailed below.

We note that the vessel-specific flow and MBF targets from MPI_{CT} were calculated relative to the total LV flow because MPI_{CT} is known to underestimate the absolute flow[12,46]. In addition, we only had MBF in the LV. So for vessels that were not perfusing the LV (proximal right coronary artery branches), we applied Murray's law boundary conditions. As a basis for comparison, we also tuned each model to match all the above clinical targets except vessel-specific flows. In these latter models, the distribution of flow amongst the coronary arteries was prescribed based on their lumen diameters using Murray's law[36,37], as is more conventionally done.

The surrogate model we used for the optimization was a lumped parameter representation of each patient-specific coronary artery anatomical model. This was generated using an automated method[80] that extracts the lumen centerlines of all vessels in the anatomy, computes vessel radii by traversing along the centerlines, and distills this information into a network of resistance-capacitance-inductance lumped parameter models for each vessel in the anatomy. As in the lumped-parameter representation of the synthetic vascular trees discussed in section iv, the resistance, capacitance and inductance of each vessel were given by linearization and Poiseuille flow simplifications of the Navier Stokes equations[80]. We henceforth refer to this as a 0D surrogate model.

The multi-stage optimization procedure tuned each model to first match patient-specific measurements of cardiac function and then patient-specific flow distributions informed by MPI_{CT} (the latter was not applicable to Murray's law-based models). For all the models, the initial guess for the total vascular resistance for each patient was determined from the clinically measured average aortic pressure divided by cardiac output. The total coronary flow was given by the morphometric scaling with the LV volume, $Q_{LV} = 3.41 \times V_{LV}^{0.75}$ mL/min for branches perfusing the LV and $0.2 \times Q_{LV}$ for other branches[46,49,90,91]. For the models tuned to match the flow distribution measured by MPI_{CT}, the total coronary resistance was initially distributed amongst the branches of the coronary tree based on the ratio of total MBF to vessel-specific MBF for each vessel. On the other hand, for the models tuned to match flow distributions resulting from Murray's law, the total coronary resistance was distributed amongst all coronary branches based on their diameters scaled to an exponent of 2.6[37]. This was done for coronary arteries that were image-based as well as outlets of the synthetic vessels. The total capacitance was set as 0.28×10^{-3} cm^5/dynes for aortic branches and 10^{-6} cm^5/dynes for coronary branches based on previous work[82]. The total capacitance was distributed amongst branches to be proportional to their outlet areas[90]. When tuning all the models, the permissible range for each parameter was assigned based on physiological values and the initial guess was based on the maximum posterior of the distribution of parameters computed using Markov Chain Monte Carlo techniques in our previous work using similar closed-loop LPN models for coronary hemodynamics[83].

Optimizing for cardiac function. In the first stage we optimized the parameters of the closed-loop system to match all the above clinical targets except the vessel-specific flows. This consisted of 36 parameters governing the hemodynamics and function of the four heart chambers, the pulmonary circulation, the intramyocardial pressure experienced by coronary arteries, and the total distal resistance and capacitance at all the aortic and coronary outlets. For details about the parameters optimized in this stage, see reference[74]. This optimization was performed using the Nelder-Mead method, a deterministic gradient-free optimization technique[92]. The convergence tolerance for the optimization was 0.1, maximum number of iterations was 200, the parameter update step size was 0.1 of the range for each parameter, and the number of restarts was 50.

Optimizing for blood flow distribution: without synthetic vasculature. The second stage of optimization focused on vessel-specific outlet boundary conditions. In this stage, we kept the 36 parameters that were optimized in the first stage fixed, and tuned the outlet resistances (represented by R_a, R_μ and R_v in Fig. 2d) of all the branches in the coronary tree to match clinically measured flow distributions from MPI_{CT}.

For the models that were not augmented with synthetic vascular trees, this consisted of two parameters for each of the $N_{outlets}^{CT}$ coronary outlets perfusing the LV – the total outlet resistance for each branch ($R_a^i + R_\mu^i + R_v^i$, where $i = 1, \ldots, N_{outlets}^{CT}$ is the index of the outlet), and the ratio of proximal vessel to microvascular resistance at each outlet (R_a^i/R_μ^i). The former determines the flow distribution in the coronary tree while the latter dictates the distribution of microvascular pressure that drives myocardial perfusion. We first used Nelder-Mead optimization to tune the relative distribution of total resistance amongst all the coronary artery outlets so that the resulting distribution of flow in the coronary tree matched that measured from MPI_{CT}. This was done using a $N_{outlets}^{CT}$-dimensional optimization procedure that estimated a scaling factor constrained to the range [0.5, 2.0] for the resistance at each outlet, such that the total outlet resistance of the model was kept equal to the value obtained from the first stage of optimization. The convergence tolerance for the error was set to 0.1, the maximum number of iterations was 200, the parameter update step size was 0.1 of the range, and the number of restarts was 50.

We then fixed the total resistance of the complete tree as well as the total resistance at each outlet, and estimated the ratio of proximal to microvascular resistance that matched the required distribution of microvascular pressure. Note that the required microvascular pressure source (p_{src} in Eq. (2)) in each vessel-specific perfusion territory can be computed from Eq. (4). This is given by $p_{src}^i = MBF_{V_i}/(\beta_{src} V_i) + p_{cap}$, where a guess for all the pressure sources is required to compute $\bar{p}_{src}$ in β_{src}. In addition, the simulated microvascular pressure at each outlet i in the flow simulation is given by $P_\mu^i = P^i - Q^i R_a^i$, where P^i and Q^i are the pressure and flow at outlet i (see Fig. 2d). We therefore ran a 3D simulation with deformable walls to estimate the outlet pressure P^i and microvascular pressure P_μ^i at each coronary outlet. For this initial simulation, we assumed the ratio of proximal to microvascular resistance was $R_a^i/R_\mu^i = 0.38$ at each outlet, following previous work[74,82]. This computation of the pressure loss along each branch, combined with the required p_{src}^i for each branch, informed a direct update of R_a^i/R_μ^i at each outlet to obtain the required microvascular pressure. This updated ratio of proximal to microvascular resistance, along with the optimized distribution of outlet resistances, was then used to run a 3D simulation with deformable walls at hyperemia. The microvascular pressure obtained at each outlet from this simulation, along with the required microvascular pressure source for each outlet from Eq. (4), was then used to inform a second update of the ratio between the proximal and microvascular resistance at each coronary outlet. We note that while we have discussed the estimation of microvascular resistances in the context of the outlet boundary condition at each coronary artery above, this also implicitly estimates β_{src} and p_{src}, which are parameters governing the myocardial blood flow model in Eq. (2).

Optimizing for blood flow distribution: with synthetic vasculature. For the models augmented with synthetic vascular trees, a different approach was employed for tuning the boundary conditions at the outlets, since these models consisted of $N_{outlets}^{syn} = 500$ coronary outlets (compared to ~16 outlets without synthetic vasculature), rendering the approach above computationally intractable. Moreover, since the synthetic trees generated by CCO are not patient-specific, we noticed that the vascular resistance along some paths from the aorta to outlet vessels led to unphysiological outlet boundary conditions (such as negative resistance) in order to match clinically measured flow and pressure distributions. Therefore, we developed a novel iterative approach to personalizing synthetic vasculature that estimates not only the parameters at the coronary outlets, but also dilates or constricts the synthetic vessels to match patient-specific flow and pressure targets.

Each iteration of the procedure consisted of: (1) sub-iterations to match the required flow distributions in the 0D surrogate to within 5% error, which involved updating the distal resistance boundary condition at each outlet vessel and dilating the synthetic vascular trees if unphysiological negative resistances were required to match the flow targets; (2) a simulation of the updated surrogate model and comparison of the outlet pressure distribution with that required to match clinically imaged MBF; (3) the dilation or constriction of all the synthetic vascular trees to obtain the required pressure distribution if the average pressure error was greater than 5%. The above steps were iterated upon until both the flow and pressure errors (based on the 0D surrogate model) were below 5%. Each of these steps is described in detail below.

With the parameters derived from the first stage of optimization, we first ran a 0D simulation at hyperemia to compute the pressure at all outlets. Using the aortic pressure and outlet pressures, we estimated the linear vascular resistance along each path from the aortic inlet to a coronary outlet, given by $R_{path}^i = (P_{aorta} - P^i)/Q^i$, where P^i and Q^i are the pressure and flow at an outlet synthetic vessel indexed by i. We also computed the resistance of the paths from each outlet of the image-based epicardial vessels to all outlets of the synthetic tree that was appended to that epicardial vessel. This is given by $R_{path,syn}^i = (P_{epi}^i - P^i)/Q^i$ where P_{epi}^i is the pressure at the outlet of the image-based epicardial vessel which is upstream of the synthetic vessel outlet i.

Given the resistance R_{path}^i along each aorta-to-outlet path and the total resistance of the model estimated from the first stage of optimization (R_{tot}), we calculated the required resistance distal to each outlet as $R_{out,reqd}^i = R_{tot} Q_{LV}/Q_{reqd}^i - R_{path}^i$, where Q_{reqd}^i is the target flow through outlet i, according to MPI_{CT}. This informed an updated resistance distal to each outlet. For some outlets in the model, this estimated outlet resistance

was negative. This was due to excessive pressure drop along the path from the aorta to outlet i, i.e. R^i_{path} was too large. Since each R^i_{path} consisted of the sum of resistance from the upstream image-based epicardial vessels and downstream synthetic vessels, we addressed this by dilating the synthetic vascular trees. This achieved the required resistance along each path while maintaining the anatomy of the upstream branches that were based on patient-specific imaging. For each $R^i_{out,reqd}$ that was negative, we estimated the required resistance of the path from the outlet of the corresponding image-based vessel to the synthetic outlet i, which we denote as $\tilde{R}^i_{path,syn}$, such that $R^i_{out,reqd}>0$. Note that $\tilde{R}^i_{path,syn}<R^i_{path,syn}$, since we are aiming to decrease R^i_{path}. Each of these synthetic vessel outlets was then assigned a radius scaling factor to achieve this reduced resistance, given by $\alpha^i=(R^i_{path,syn}/\tilde{R}^i_{path,syn})^{1/4}>1$. The synthetic trees were then dilated using the method described below. The above procedure was iteratively performed until physiological outlet resistances were attained for each synthetic vessel outlet and the average error in the outlet flow fractions, $\epsilon_{flow}=\sum_i(|Q^i-Q^i_{reqd}|/Q^i_{reqd})/N^{syn}_{outlets}$, was less than 5%.

We scaled the radii of synthetic vessels after each outlet vessel was assigned a radius scaling factor, α^i, by traversing up each synthetic tree from the outlet vessels to the root of the tree. As we traversed up the tree, each parent vessel was assigned a scaling factor that was the maximum of the scaling factors of its two daughter vessels. Moreover, the maximum scaling factor for each vessel was constrained by the radius of its parent vessel. This ensured the preservation of the morphometric structure of the tree. In this way, each vessel in every vascular tree was assigned a scaling factor α^i by propagating the outlet vessel scaling factors up the tree. We then updated the resistance, inductance and capacitance values of all the synthetic vessels based on the new radius.

Once the outlet boundary conditions were updated through the above procedure, we tuned the vascular resistance of the synthetic vasculature to obtain the required microvascular pressure distribution at the coronary outlets based on the MBF distribution from MPI_{CT}. As discussed in section vii.2, the target microvascular pressure source at each coronary outlet (p_{src} in Eq. (2)) can be estimated from Eq. (4). This is given by $p^i_{src}=MBF_{V_i}/(\beta_{src}V_i)+p_{cap}$. Therefore, the target pressure at every synthetic vessel outlet with index i can be calculated as $P^i_{reqd}=p^i_{src}+Q^i_{reqd}R^i_a$. Furthermore, the required vascular resistance along each path from the aortic inlet to each synthetic vessel outlet can be calculated from the required outlet pressure and required outlet flow, $R^i_{path,reqd}=(P_{aorta}-P^i_{reqd})/Q^i_{reqd}$. Therefore, we ran a second 0D simulation at hyperemia to estimate the pressure at all the synthetic vessel outlets. We computed the average relative pressure error over all the outlets as $\epsilon_{pressure}=\sum_i(|P^i-P^i_{reqd}|/P^i_{reqd})/N^{syn}_{outlets}$. If this error was greater than 5%, we proceeded as follows to update the resistance of synthetic vascular trees. The 0D simulation again allowed us to calculate the path-specific vascular resistance from the aortic inlet to each synthetic tree outlet (R^i_{path}). Similarly, we calculated the resistance from each image-based epicardial coronary outlet to the synthetic vessel outlets that were appended to that image-based vessel ($R^i_{path,syn}$). Given the required resistance along each path computed above ($\tilde{R}^i_{path,reqd}$), and the separate contributions to this resistance from the image-based vessels and synthetic vessels (R^i_{path} and $R^i_{path,syn}$), we computed the required vascular resistance of the synthetic vessels along the path from the outlet of the corresponding upstream image-based vessel to the synthetic outlet i. This resistance, denoted by $\tilde{R}^i_{path,syn}$, then informs a radius scaling factor $\alpha_i=(R^i_{path,syn}/\tilde{R}^i_{path,syn})^{1/4}$ for the each synthetic vessel outlet i. We constrict/dilate the synthetic vascular trees using the procedure described above, and then return to the start of the iteration to estimate new outlet resistances and the flow distribution resulting from this updated anatomy.

Data availability

All computational models built for this study have been anonymized and made publicly available through the Vascular Model Repository (www.vascularmodel.com).

Code availability

The patient-specific modeling pipeline and computational fluid dynamics solvers are part of the *SimVascular* open-source project (www.simvascular.github.io). Image analysis and postprocessing was also performed using the open-source tools specified in the section titled Clinical imaging protocols and processing.

Received: 22 August 2023; Accepted: 25 February 2024;
Published online: 01 May 2024

References

1. Tsao, C. W. et al. Heart Disease and Stroke Statistics-2022 Update: A Report from the American Heart Association. *Circulation* **145**, E153–E639 (2022).
2. Ralapanawa, U. & Sivakanesan, R. Epidemiology and the magnitude of coronary artery disease and acute coronary syndrome: A narrative review. *J. Epidemiol. Global Health* **11**, 169–177 (2021).
3. Yusuf, S. et al. Effect of coronary artery bypass graft surgery on survival: overview of 10-year results from randomised trials by the Coronary Artery Bypass Graft Surgery Trialists Collaboration. *Lancet* **344**, 563–570 (1994).
4. Windecker, S. et al. Revascularisation versus medical treatment in patients with stable coronary artery disease: Network meta-analysis. *BMJ* **348**, https://www.bmj.com/content/348/bmj.g3859, https://www.bmj.com/content/348/bmj.g3859.abstract (2014).
5. Velazquez, E. J. et al. Coronary-Artery Bypass Surgery in Patients with Ischemic Cardiomyopathy. *N. Engl. J. Med.* **374**, 1511–1520 (2016).
6. Cameron, A. A., Davis, K. B. & Rogers, W. J. Recurrence of angina after coronary artery bypass surgery: Predictors and prognosis (CASS registry). *J. Am. Coll. Cardiol.* **26**, 895–899 (1995).
7. Motwani, J. G. & Topol, E. J. Aortocoronary saphenous vein graft disease: Pathogenesis, predisposition, and prevention. *Circulation* **97**, 916–931 (1998).
8. Pijls, N. H. et al. Measurement of Fractional Flow Reserve to Assess the Functional Severity of Coronary-Artery Stenoses. *N. Engl. J. Med.* **334**, 1703–1708 (1996).
9. Di Carli, M. F. et al. Clinical myocardial perfusion PET/CT. *J. Nucl. Med.* **48**, 783–793 (2007).
10. Coelho-Filho, O. R., Rickers, C., Kwong, R. Y. & Jerosch-Herold, M. MR myocardial perfusion imaging. *Radiology* **266**, 701–715 (2013).
11. Danad, I., Szymonifka, J., Schulman-Marcus, J. & Min, J. K. Static and dynamic assessment of myocardial perfusion by computed tomography. *Eur. Heart J. Cardiovasc. Imaging* **17**, 836–844 (2016).
12. Nieman, K. & Balla, S. Dynamic CT myocardial perfusion imaging. *J. Cardiovas. Computed Tomogr.* **14**, 303–306 (2020).
13. Tonino, P. A. et al. Fractional flow reserve versus angiography for guiding percutaneous coronary intervention. *N. Engl. J. Med.* **360**, 213–223 (2009).
14. Pijls, N. H. et al. Fractional flow reserve versus angiography for guiding percutaneous coronary intervention in patients with multivessel coronary artery disease: 2-Year follow-up of the FAME (fractional flow reserve versus angiography for multivessel evaluation) study. *J. Am. Coll. Cardiol.* **56**, 177–184 (2010).
15. Underwood, S. R., Godman, B., Salyani, S., Ogle, J. R. & Ell, P. J. Economics of myocardial perfusion imaging in Europe - The EMPIRE study. *Eur. Heart J.* **20**, 157–166 (1999).
16. Bamberg, F. et al. Detection of hemodynamically significant coronary artery stenosis: Incremental diagnostic value of dynamic CT-based myocardial perfusion imaging. *Radiology* **260**, 689–698 (2011).
17. Giordano, M. et al. Classification of hemodynamically significant stenoses from dynamic CT perfusion and CTA myocardial territories:. *Med. Phys.* **44**, 1347–1358 (2017).
18. Lubbers, M. et al. Comprehensive Cardiac CT With Myocardial Perfusion Imaging Versus Functional Testing in Suspected Coronary

Artery Disease: The Multicenter, Randomized CRESCENT-II Trial. *JACC Cardiovasc. Imaging* **11**, 1625–1636 (2018).
19. Meijboom, W. B. et al. Diagnostic Accuracy of 64-Slice Computed Tomography Coronary Angiography: A Prospective, Multicenter, Multivendor Study. *J. Am. Coll. Cardiol.* **52**, 2135–2144 (2008).
20. Meijboom, W. B. et al. Comprehensive Assessment of Coronary Artery Stenoses: Computed Tomography Coronary Angiography Versus Conventional Coronary Angiography and Correlation With Fractional Flow Reserve in Patients With Stable Angina. *J. Am. Coll. Cardiol.* **52**, 636–643 (2008).
21. Marsden, A. L. Optimization in cardiovascular modeling. *Ann. Rev. Fluid Mech.* **46**, 519–546 (2014).
22. Taylor, C. A., Fonte, T. A. & Min, J. K. Computational fluid dynamics applied to cardiac computed tomography for noninvasive quantification of fractional flow reserve: Scientific basis. *J. Am. Coll. Cardiol.* **61**, 2233–2241 (2013).
23. Koo, B. K. et al. Diagnosis of ischemia-causing coronary stenoses by noninvasive fractional flow reserve computed from coronary computed tomographic angiograms: Results from the prospective multicenter DISCOVER-FLOW (Diagnosis of Ischemia-Causing Stenoses Obtained Via Noni. *J. Am. Coll. Cardiol.* **58**, 1989–1997 (2011).
24. Min, J. K. et al. Diagnostic accuracy of fractional flow reserve from anatomic CT angiography. *JAMA* **308**, 1237–1245 (2012).
25. Karády, J. et al. Cost-effectiveness Analysis of Anatomic vs Functional Index Testing in Patients With Low-Risk Stable Chest Pain. *JAMA Network. Open* **3**, e2028312–e2028312 (2020).
26. Morbiducci, U., Ponzini, R., Grigioni, M. & Redaelli, A. Helical flow as fluid dynamic signature for atherogenesis risk in aortocoronary bypass. A numeric study. *J. Biomech.* **40**, 519–534 (2007).
27. Ramachandra, A. B., Sankaran, S., Humphrey, J. D. & Marsden, A. L. Computational Simulation of the Adaptive Capacity of Vein Grafts in Response to Increased Pressure. *J. Biomech. Eng.* **137**, 1–10 (2015).
28. Ramachandra, A. B., Kahn, A. M. & Marsden, A. L. Patient-Specific Simulations Reveal Significant Differences in Mechanical Stimuli in Venous and Arterial Coronary Grafts. *J. Cardiovasc. Transl. Res.* **9**, 279–290 (2016).
29. Ramachandra, A. B., Humphrey, J. D. & Marsden, A. L. Gradual loading ameliorates maladaptation in computational simulations of vein graft growth and remodelling. *J. R. Soc. Interface* **14**, 20160995 (2017).
30. Khan, M. O. et al. Low Wall Shear Stress Is Associated with Saphenous Vein Graft Stenosis in Patients with Coronary Artery Bypass Grafting. *J. Cardiovasc. Transl. Res.* **14**, 770–781 (2020).
31. Ramachandra, A. B. et al. Biodegradable external wrapping promotes favorable adaptation in an ovine vein graft model. *Acta Biomaterialia* **151**, 414–425 (2022).
32. Candreva, A. et al. Risk of myocardial infarction based on endothelial shear stress analysis using coronary angiography. *Atherosclerosis* **342**, 28–35 (2022).
33. Shanbhag, S. M. & Chen, M. Y. Ultra-High-Resolution Coronary CT Angiography: The "Final Frontier"–Are We There Yet?*Radiology* **3**, https://www.ncbi.nlm.nih.gov/pmc/articles/PMC8415137/ (2021).
34. Wellnhofer, E. et al. Flow simulation studies in coronary arteries-Impact of side-branches. *Atherosclerosis* **213**, 475–481 (2010).
35. Vardhan, M. et al. The importance of side branches in modeling 3D hemodynamics from angiograms for patients with coronary artery disease. *Sci. Rep.* **9**, 1–10 (2019).
36. Murray, C. D. The Physiological Principle of Minimum Work 1: The Vascular System and the Cost of Blood Volume. *Proc. Natl Acad. Sci.* **12**, 207–214 (1926).
37. Zhou, Y., Kassab, G. S. & Molloi, S. On the design of the coronary arterial tree: A generalization of Murray's law. *Phys. Med. Biol.* **44**, 2929–2945 (1999).
38. van der Giessen, A. G. et al. The influence of boundary conditions on wall shear stress distribution in patients specific coronary trees. *J. Biomech.* **44**, 1089–1095 (2011).
39. Berthier, B., Bouzerar, R. & Legallais, C. Blood flow patterns in an anatomically realistic coronary vessel: Influence of three different reconstruction methods. *J. Biomech.* **35**, 1347–1356 (2002).
40. Schrauwen, J. T. et al. Functional and anatomical measures for outflow boundary conditions in atherosclerotic coronary bifurcations. *J. Biomech.* **49**, 2127–2134 (2016).
41. Sankaran, S., Kim, H. J., Choi, G. & Taylor, C. A. Uncertainty quantification in coronary blood flow simulations: Impact of geometry, boundary conditions and blood viscosity. *J. Biomech.* **49**, 2540–2547 (2016).
42. Maher, G., Fleeter, C., Schiavazzi, D. & Marsden, A. Geometric Uncertainty in Patient-Specific Cardiovascular Modeling with Convolutional Dropout Networks. *Comput. Methods Appl. Mech. Eng.* **386**, 114038 (2020).
43. Seo, J., Schiavazzi, D. E., Kahn, A. M. & Marsden, A. L. The effects of clinically-derived parametric data uncertainty in patient-specific coronary simulations with deformable walls. *Int. J. Numer. Methods Biomed. Eng.* **36**, 1–27 (2020).
44. Lodi Rizzini, M. et al. Modelling coronary flows: impact of differently measured inflow boundary conditions on vessel-specific computational hemodynamic profiles. *Comput. Methods Progr. Biomed.* **221**, 106882 (2022).
45. Nous, F. M. et al. Dynamic Myocardial Perfusion CT for the Detection of Hemodynamically Significant Coronary Artery Disease. *JACC Cardiovasc. Imaging* **15**, 75–87 (2022).
46. Xue, X. et al. Personalized coronary blood flow model based on CT perfusion to non-invasively calculate fractional flow reserve. *Comput. Methods Appl. Mech. Eng.* **404**, 115789 (2023).
47. Schreiner, W. & Buxbaum, P. F. Computer-Optimization of Vascular Trees. *IEEE Trans. Biomed. Eng.* **40**, 482–491 (1993).
48. Jaquet, C. et al. Generation of Patient-Specific Cardiac Vascular Networks: A Hybrid Image-Based and Synthetic Geometric Model. *IEEE Trans. Biomed. Eng.* **66**, 946–955 (2019).
49. Papamanolis, L. et al. Myocardial Perfusion Simulation for Coronary Artery Disease: A Coupled Patient-Specific Multiscale Model. *Ann. Biomed. Eng.* **49**, 1432–1447 (2021).
50. Kim, H. J., Rundfeldt, H. C., Lee, I. & Lee, S. Tissue-growth-based synthetic tree generation and perfusion simulation. *Biomech. Model. Mechanobiol.* **22**, 1095–1112 (2023).
51. Chapelle, D., Gerbeau, J. F., Sainte-Marie, J. & Vignon-Clementel, I. E. A poroelastic model valid in large strains with applications to perfusion in cardiac modeling. *Comput. Mech.* **46**, 91–101 (2010).
52. Cookson, A. N. et al. A novel porous mechanical framework for modelling the interaction between coronary perfusion and myocardial mechanics. *J. Biomech.* **45**, 850–855 (2012).
53. Hyde, E. R. et al. Multi-scale parameterisation of a myocardial perfusion model using whole-organ arterial networks. *Ann. Biomed. Eng.* **42**, 797–811 (2014).
54. Di Gregorio, S. et al. A computational model applied to myocardial perfusion in the human heart: From large coronaries to microvasculature. *J. Comput. Phys.* **424**, 109836 (2021).
55. Di Gregorio, S. et al. Prediction of myocardial blood flow under stress conditions by means of a computational model. *Eur. J. Nucl. Med. Mol. Imaging* **49**, 1894–1905 (2022).
56. Nakazato, R. et al. Noninvasive fractional flow reserve derived from computed tomography angiography for coronary lesions of intermediate stenosis severity results from the DeFACTO study. *Circulation* **6**, 881–889 (2013).
57. Kassab, G. S., Rider, C. A., Tang, N. J. & Fung, Y. C. Morphometry of pig coronary arterial trees. *Am. J. Physiol. Heart Circ. Physiol.* **265**, 350–365 (1993).

58. Yang, W., Feinstein, J. A. & Vignon-Clementel, I. E. Adaptive outflow boundary conditions improve post-operative predictions after repair of peripheral pulmonary artery stenosis. *Biomech. Model. Mechanobiol.* **15**, 1345–1353 (2016).
59. Schwarz, E. L. et al. Hemodynamic performance of tissue-engineered vascular grafts in Fontan patients. *npj Regen. Med.* **6**, https://doi.org/10.1038/s41536-021-00148-w (2021).
60. De Bruyne, B. et al. Microvascular Resistance Reserve for Assessment of Coronary Microvascular Function: JACC Technology Corner. *J. Am. Coll. Cardiol.* **78**, 1541–1549 (2021).
61. Seo, J., Fleeter, C., Kahn, A. M., Marsden, A. L. & Schiavazzi, D. E. Multi-fidelity estimators for coronary circulation models under clinically-informed data uncertainty. *Int. J. Uncertainty Quantif.* **10**, 449–466 (2019).
62. Fleeter, C. M., Geraci, G., Schiavazzi, D. E., Kahn, A. M. & Marsden, A. L. Multilevel and multifidelity uncertainty quantification for cardiovascular hemodynamics. *Comput. Methods Appl. Mech. Eng.* **365**, 113030 (2020).
63. Zanoni, A. et al. Improved multifidelity Monte Carlo estimators based on normalizing flows and dimensionality reduction techniques. arXiv:2312.12361 (2023).
64. Humphrey, J. D., Dufresne, E. R. & Schwartz, M. A. Mechanotransduction and extracellular matrix homeostasis. *Nat. Rev. Mol. Cell Biol.* **15**, 802–812 (2014).
65. Spaan, J. A. et al. Visualisation of intramural coronary vasculature by an imaging cryomicrotome suggests compartmentalisation of myocardial perfusion areas. *Med. Biol. Eng. Comput.* **43**, 431–435 (2005).
66. Mahnken, A. H. et al. Quantitative whole heart stress perfusion ct imaging as noninvasive assessment of hemodynamics in coronary artery stenosis: Preliminary animal experience. *Investig. Radiol.* **45**, 298–305 (2010).
67. Si, H. TetGen, a Delaunay-Based Quality Tetrahedral Mesh Generator. *ACM Trans. Math. Softw.* **41**, https://doi.org/10.1145/2629697 (2015).
68. Updegrove, A. et al. SimVascular: An Open Source Pipeline for Cardiovascular Simulation. *Ann. Biomed. Eng.* **45**, 525–541 (2017).
69. Jansen, K., Whiting, C. & Hulbert, G. A generalized-a method for integrating the filtered Navier-Stokes equations with a stabilized finite element method. *Comput. Methods Appl. Mech. Eng.* **190**, 305–320 (1999).
70. Whiting, C. H. & Jansen, K. E. A stabilized finite element method for the incompressible Navier-Stokes equations using a hierarchical basis. *Int. J. Numer. Methods Fluids* **35**, 93–116 (2001).
71. Secomb, T. W. Blood Flow in the Microcirculation. *Ann. Rev. Fluid Mech.* **49**, 443–461 (2017).
72. Figueroa, C. A., Vignon-Clementel, I. E., Jansen, K. E., Hughes, T. J. & Taylor, C. A. A coupled momentum method for modeling blood flow in three-dimensional deformable arteries. *Comput. Methods Appl. Mech. Eng.* **195**, 5685–5706 (2006).
73. Grande Gutierrez, N. et al. Hemodynamic variables in aneurysms are associated with thrombotic risk in children with Kawasaki disease. *Int. J. Cardiol.* **281**, 15–21 (2019).
74. Menon, K. et al. Predictors of Myocardial Ischemia in Patients with Kawasaki Disease: Insights from Patient-Specific Simulations of Coronary Hemodynamics. *J. Cardiovasc. Transl. Res.* **16**, 1099–1109 (2023).
75. Gow, B. S. & Hadfield, C. D. The elasticity of canine and human coronary arteries with reference to postmortem changes. *Circ. Res.* **45**, 588–594 (1979).
76. Coogan, J. S., Humphrey, J. D. & Figueroa, C. A. Computational simulations of hemodynamic changes within thoracic, coronary, and cerebral arteries following early wall remodeling in response to distal aortic coarctation. *Biomech. Model. Mechanobiol.* **12**, 79–93 (2013).
77. Roccabianca, S., Figueroa, C. A., Tellides, G. & Humphrey, J. D. Quantification of regional differences in aortic stiffness in the aging human. *J. Mech. Behav. Biomed. Mater.* **29**, 618–634 (2014).
78. Podesser, B. K. et al. Outer Radius-Wall Thickness Ratio, a Postmortem Quantitative Histology in Human Coronary Arteries. *Acta Anatomica* **163**, 63–68 (1998).
79. Sexton, Z. A. et al. Rapid model-guided design of organ-scale synthetic vasculature for biomanufacturing. *arXiv*, http://arxiv.org/abs/2308.07586 (2023).
80. Pfaller, M. R. et al. Automated generation of 0D and 1D reduced-order models of patient-specific blood flow. *Int. J. Numer. Methods Biomed. Eng.* **38**, e3639 (2022).
81. Esmaily Moghadam, M., Vignon-Clementel, I. E., Figliola, R. & Marsden, A. L. A modular numerical method for implicit 0D/3D coupling in cardiovascular finite element simulations. *J. Comput. Phys.* **244**, 63–79 (2013).
82. Sankaran, S. et al. Patient-specific multiscale modeling of blood flow for coronary artery bypass graft surgery. *Ann. Biomed. Eng.* **40**, 2228–2242 (2012).
83. Tran, J. S., Schiavazzi, D. E., Ramachandra, A. B., Kahn, A. M. & Marsden, A. L. Automated tuning for parameter identification and uncertainty quantification in multi-scale coronary simulations. *Comput. Fluids* **142**, 128–138 (2017).
84. Vignon-Clementel, I. E., Alberto Figueroa, C., Jansen, K. E. & Taylor, C. A. Outflow boundary conditions for three-dimensional finite element modeling of blood flow and pressure in arteries. *Comput. Methods Appl. Mech. Eng.* **195**, 3776–3796 (2006).
85. Kim, H. J. et al. Patient-specific modeling of blood flow and pressure in human coronary arteries. *Ann. Biomed. Eng.* **38**, 3195–3209 (2010).
86. Esmaily-Moghadam, M., Hsia, T. Y. & Marsden, A. L. A non-discrete method for computation of residence time in fluid mechanics simulations. *Phys. Fluids* **25**, 1–21 (2013).
87. Wilson, R. F., Wyche, K., Christensen, B. V., Zimmer, S. & Laxson, D. D. Effects of adenosine on human coronary arterial circulation. *Circulation* **82**, 1595–1606 (1990).
88. Kovacs, G., Berghold, A., Scheidl, S. & Olschewski, H. Pulmonary arterial pressure during rest and exercise in healthy subjects: A systematic review. *Eur. Respir. J.* **34**, 888–894 (2009).
89. Ofili, E. O. et al. Differential characterization of blood flow, velocity, and vascular resistance between proximal and distal normal epicardial human coronary arteries: Analysis by intracoronary Doppler spectral flow velocity. *Am. Heart J.* **130**, 37–46 (1995).
90. Choy, J. S. & Kassab, G. S. Scaling of myocardial mass to flow and morphometry of coronary arteries. *J. Appl. Physiol.* **104**, 1281–1286 (2008).
91. Crystal, G. J. & Pagel, P. S. Physiology and Clinical Implications. *Anesthesiology* **128**, 202–218 (2018).
92. Nelder, J. A. & Mead, R. A Simplex Method for Function Minimization. *Comput. J.* **7**, 308–313 (1965).

Acknowledgements

This work was supported by NIH grant R01HL141712 and the Additional Ventures Cures Collaborative. Z.A.S. was funded by the NSF Graduate Research Fellowship Program (DGE-1656518). High performance computing resources were provided by XSEDE and the Stanford Research Computing Center.

Author contributions

K.M. wrote the analysis and modeling codes, performed the analysis, prepared figures and wrote the manuscript. M.O.K. contributed image analysis tools. Z.A.S. and J.R. contributed modeling tools. K.N., P.K.N. S.B.M. and J.B. collected clinical data. K.M., K.N. and A.L.M. conceived and designed the analysis. K.N. and A.L.M. acquired funding.

Competing interests
The authors declare no competing interests.

Additional information
Supplementary information The online version contains supplementary material available at https://doi.org/10.1038/s44303-024-00014-6.

Correspondence and requests for materials should be addressed to Alison L. Marsden.